Journal of Sound and Vibration 330 (2011) 843–867

Contents lists available at ScienceDirect

Journal of Sound and Vibration

journal homepage: www.elsevier.com/locate/jsvi

Comparison of decentralized velocity feedback control for thin homogeneous and stiff sandwich panels using electrodynamic proof-mass actuators

J. Rohlfing [a,*], P. Gardonio [b], D.J. Thompson [a]

[a] Institute of Sound and Vibration Research, University of Southampton, Southampton S017 1BJ, UK
[b] DIEGM, Università degli Studi di Udine, Via delle Scienze, 208 33100 Udine, Italy

ARTICLE INFO

Article history:
Received 13 March 2010
Received in revised form
12 August 2010
Accepted 16 September 2010
Handling Editor: D.J. Wagg
Available online 15 October 2010

ABSTRACT

Theoretical and experimental work is presented to compare the effect of decentralised velocity feedback control on thin homogeneous and sandwich panels. The decentralised control system consists of five control units, which are composed of a proof-mass electrodynamic actuator with an accelerometer underneath its footprint and an analogue controller. The stability of the feedback loops is analysed by considering the sensor-actuator open-loop frequency response function of each control unit and the eigenvalues of the fully populated matrix of open-loop frequency response functions between the five sensors and five actuators. The control performance is then analysed in terms of the time-averaged total kinetic energy and total sound power radiated by the two panels. The results show that for a stiff sandwich panel higher stable feedback gains can be implemented than on a thin homogeneous panel of comparable weight per unit area. Moreover the implementation of decentralised velocity feedback can offset some of the undesirable sound transmission properties of lightweight sandwich structures by efficiently reducing structural vibration and sound power radiation in the mid audio frequency range.

1. Introduction

The need to tackle the current problems of fossil fuel stock decline and climate change is causing an increasing interest in lightweight design for fuel efficient vehicles. Honeycomb sandwich panels are very appealing for lightweight constructions due to their high stiffness to weight ratio. However, the reduced mass per unit area and the shift of the acoustic critical frequency into the mid audio frequency range are likely to cause an increase in sound transmission and hence in vehicle interior noise levels.

Aircraft and car manufacturers have already started to investigate innovative lightweight designs for the fuselage of aircraft and for car body shells. In order to maintain structural strength, these designs increasingly involve stiff and lightweight panels. Unfortunately these have undesirable acoustic properties and efficiently transmit noise from various external airborne and structure-borne sources [1–4] into the vehicle interior. In particular the airframe of the new generation of aircraft involves an increasing proportion of lightweight and stiff composite materials made from carbon

* Corresponding author.
E-mail address: J.Rohlfing@soton.ac.uk (J. Rohlfing).

0022-460X/$ - see front matter © 2010 Elsevier Ltd. All rights reserved.
doi:10.1016/j.jsv.2010.09.013

fibre reinforced plastics. Car manufacturers have also begun to consider lightweight constructions, e.g. aluminium and carbon fibre car bodies, and the use of stiff lightweight sandwich panels made from low cost materials. Similarly the train industry has also introduced new designs of railway carriage using extruded aluminium frame structures and panels [5]. The use of these new materials and sandwich structures has a direct impact on the structure-borne and air-borne sound transmission.

Passive treatments, such as stiffening, mass or damping treatments, can be used to reduce the undesired effects in the dynamic response of stiffened lightweight structures at mid and high audio frequencies. At these frequencies the response of the structures is characterised by a large number of resonant modes that overlap (typical frequency range of interest up to 5000 Hz). However, in many cases, in order to be effective at low audio frequencies, where the response of the structures and interior acoustic cavities tends to be characterised by a low number of well-separated resonant modes, passive treatments tend to be bulky and add a considerable amount of extra mass, which interferes with the weight requirements for these vehicles [6–8]. In general it is this 'low' frequency range (typically below 500 Hz) where active control systems outperform passive treatments. However, for stiff lightweight materials this 'low' frequency range extends further into the mid-audio frequency range than for conventional structures. Active control systems can be used to develop stiff smart panels that could satisfy both the requirements for low weight and low sound transmission properties. A previous simulation study has compared decentralised velocity feedback control for thin homogeneous and lightweight sandwich panels under deterministic and stochastic excitation [9]. This indicated that velocity feedback control on stiff lightweight sandwich panels can be more efficient than on a thin aluminium panel. However, these studies assumed ideal feedback loops with collocated ideal velocity and ideal force sensor-actuator pairs, which are unconditionally stable [10]. In practice sensor-actuator pairs cannot be treated as collocated ideal transducer pairs. Hence practical control feedback loops are only conditionally stable, where the maximum stable feedback gain depends on both the dynamics of the control units and the dynamic response of the panel they are mounted on [11].

One way to generate a 'sky-hook' transverse force excitation on structures is to use electrodynamic voice coil actuators which react off a resiliently suspended proof-mass [12]. For example Paulitsch et al. [13,14] developed a compact lightweight proof-mass electrodynamic actuator and produced a prototype control unit with an accelerometer sensor located in the centre of the actuator footprint, specifically designed for velocity feedback purposes. The main stability issue for feedback loops with this type of sensor-actuator pair occurs around the actuator fundamental resonance frequency which causes a 180° phase shift in the sensor-actuator open-loop frequency response function [11]. An important factor for the stability of the feedback loop is the ratio between the resonance frequencies of the first bending mode of the panel and the fundamental resonance of the actuator. In fact the control gain margin that guarantees stability increases as the ratio between the fundamental resonance frequency of the structure under control and that of the proof-mass actuator increases [15,16].

This paper presents a comprehensive comparison of the stability properties and control performance of decentralised velocity feedback control using electrodynamic proof-mass actuators on two panels. These are a thin homogeneous aluminium panel and a stiff sandwich panel with honeycomb core. The two panels have an equivalent mass per unit area but the sandwich panel has a much higher stiffness than the aluminium panel. The passive and active effects of the control units are investigated in order to assess the feasibility and advantages of stiff smart structures compared with conventional structures. In both the theoretical and experimental work a wide audio frequency range is considered. This allows the effectiveness of the smart panels to be considered both in the low frequency range, where the response of the panels is dominated by discrete resonant modes, and in the mid to high frequency range, where the response of the panels at any frequency is characterised by multiple overlapping resonant modes and where acoustic coincidence phenomena occur.

The paper is organized in five sections: Section 2 introduces the general element-based model [11] for the structural response and radiated sound power of passive and active panels with the feedback control units. Section 3 discusses the properties and dynamic characteristics of the two panels. In particular the implication of frequency dependent anisotropic behaviour on the response of the stiff honeycomb panel is discussed with respect to the wavenumbers of propagating waves and both acoustic excitation and radiation coincidence effects. Section 4 provides a brief discussion on the dynamics of the control units with proof-mass electrodynamic actuators considered in the theoretical and experimental studies. Section 5 presents simulation studies on the implementation of the decentralised feedback control system on the two panels. The model parameters are chosen to replicate closely the experimental set-ups with the aluminium and honeycomb test panels. The stability of each control unit and whole set of five control units when mounted on the two panels is investigated with the classic and generalised Nyquist stability criterion, respectively [17,18]. The control performances are analysed in terms of the time-averaged total kinetic energy and total radiated sound power of the panels, for (a) a point force, (b) an acoustic plane wave primary excitations. The total kinetic energy provides an indication of the near field sound radiation by the panels, which is particularly relevant for the interior noise in transportation vehicles, where the passengers can be located in close proximity to radiating surfaces. Alternatively, the total radiated sound power gives an indication of the far-field sound radiation by the panels that can be used to estimate the overall excitation of vehicle interior cavities and the exterior noise produced by vehicles. Section 6 presents experimental results on the stability and control performances of the decentralised control system mounted on the two panels which are placed in the window of a sound transmission suite. In this case the control performances are assessed for a point force applied by an electrodynamic shaker and an acoustic field generated by a loudspeaker located in front of the panels.

2. Active panel model

As shown in Fig. 1(a), the two panels are modelled using an elemental approach [11]. The two test panels are assumed to be mounted in an infinite rigid baffle. On the receiving side the panels radiate in an infinite half-space, where the surrounding media is supposed to be air. Fluid loading effects and radiation losses are neglected [19]. The passive and active effects of the feedback control units have been modelled in terms of the base impedance of the electrodynamic proof-mass actuators with closed velocity feedback loops.

The steady-state responses of the panels are derived in the frequency domain assuming time-harmonic excitation of the form $\mathrm{Re}\{\tilde{F}(\omega)\exp(\mathrm{j}\omega t)\}$ where, $\tilde{F}(\omega)$ is the complex phasor of the excitation, ω is the angular frequency and $\mathrm{j}=\sqrt{-1}$. Throughout the paper $\tilde{}$ is used to identify complex, frequency-dependent functions. Assuming the system is linear, the response of the panel can be modelled with the 'two-port' block diagram shown in Fig. 1(b). This indicates that the response of the panel at the element centres and the control positions is given by the following matrix expressions [19,20]

$$\tilde{\mathbf{w}}_e = \tilde{\mathbf{Y}}_{ep}\tilde{\mathbf{F}}_p + \tilde{\mathbf{Y}}_{ec}\tilde{\mathbf{F}}_c, \tag{1}$$

$$\tilde{\mathbf{w}}_c = \tilde{\mathbf{Y}}_{cp}\tilde{\mathbf{F}}_p + \tilde{\mathbf{Y}}_{cc}\tilde{\mathbf{F}}_c, \tag{2}$$

where $\tilde{\mathbf{w}}$ are velocity vectors, $\tilde{\mathbf{Y}}$ are mobility matrices and $\tilde{\mathbf{F}}$ are force vectors. The indices e, c and p denote the centre of the elements, the control and primary excitation locations on the panel. As shown in Fig. 1(b), the vector of control forces is given by

$$\tilde{\mathbf{F}}_c = -\tilde{\mathbf{Z}}_c\tilde{\mathbf{w}}_c, \tag{3}$$

where the diagonal matrix $\tilde{\mathbf{Z}}_c$ contains the base impedances of the control units. Substituting Eq. (3) into Eqs. (1) and (2), the panel element response is found to be given by

$$\tilde{\mathbf{w}}_e = [\tilde{\mathbf{Y}}_{ep} - \tilde{\mathbf{Y}}_{ec}\tilde{\mathbf{Z}}_c(\mathbf{I}_c + \tilde{\mathbf{Y}}_{cc}\tilde{\mathbf{Z}}_c)^{-1}\tilde{\mathbf{Y}}_{cp}]\tilde{\mathbf{F}}_p, \tag{4}$$

where $\mathbf{I}_c$ is a unit matrix.

A distributed disturbance is represented by equivalent forces acting at the element centres. The terms $\tilde{\mathbf{F}}_p$, $\tilde{\mathbf{Y}}_{ep}$ and $\tilde{\mathbf{Y}}_{cp}$ are therefore replaced by $\tilde{\mathbf{F}}_e$, $\tilde{\mathbf{Y}}_{ee}$ and $\tilde{\mathbf{Y}}_{ce}$. For an acoustic plane wave excitation the elements of the force vector $\tilde{\mathbf{F}}_e$ are given by

$$\tilde{F}_{e_i}(\omega) = 2A_e\hat{p}(\omega)\mathrm{e}^{-\mathrm{j}(k_x x_i + k_y y_i)}, \tag{5}$$

where i is the index of the panel element with the centre coordinates x_i and y_i and where $\hat{p}(\omega)$ is the magnitude of the pressure phasor of the incident sound wave. Also $k_x(\omega) = k_0(\omega)\sin\theta\cos\varphi$ and $k_y(\omega) = k_0(\omega)\sin\theta\sin\varphi$, where $k_0 = \omega/c_0$ is the acoustic wavenumber in air and θ and φ are the incident elevation and azimuthal angles. Finally A_e is the area of a panel element and the factor 2 accounts for the assumption of blocked forces on the panel surface. The time-averaged total kinetic energy and total radiated sound power of the panels are given by [11,20]

$$E(\omega) = \frac{M_e}{4}\tilde{\mathbf{w}}_e^H(\omega)\tilde{\mathbf{w}}_e(\omega), \tag{6}$$

$$P(\omega) = \tilde{\mathbf{w}}_e^H(\omega)\mathbf{R}_{\mathrm{rad}}(\omega)\tilde{\mathbf{w}}_e(\omega), \tag{7}$$

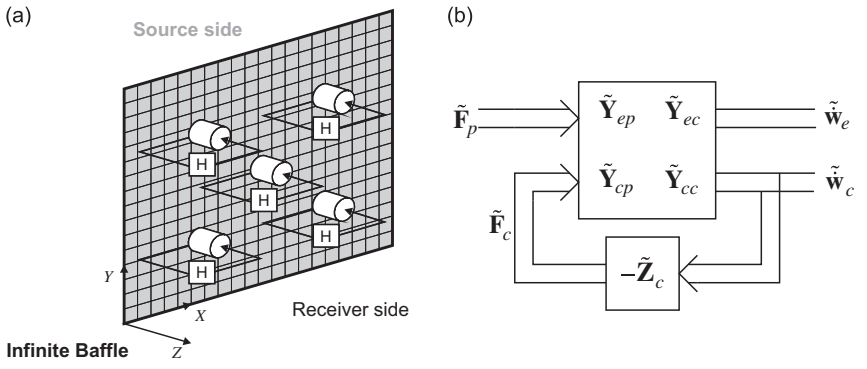

Fig. 1. (a) Panel schematic with control locations and 16×20 element grid. (b) Block diagram for multi-channel velocity feedback control.

where ^{H} denotes the hermitian transpose and where M_e is the mass of a single panel element and $\mathbf{R}_{\mathrm{rad}}(\omega)$ is the radiation matrix with the elements

$$R_{\mathrm{rad}_{i,j}} = \frac{\omega^2 \rho_0 A_e^2}{4\pi c_0} \frac{\sin(k_0 R_{i,j})}{k_0 R_{i,j}}, \tag{8}$$

where $\rho_0 = 1.21\,\mathrm{kg\,m^{-3}}$ and $c_0 = 343\,\mathrm{ms^{-1}}$ are the density and speed of sound in air and $R_{i,j}$ is the distance between the ith and jth element centre coordinates.

3. The test panels

The two panels considered in this study are shown in Fig. 2. The aluminium panel, shown in Fig. 2(a), is 1.6 mm thick and modelled as a thin homogeneous and isotropic plate using the geometry and material properties given in Table 1. In order to replicate the experimental set-up, it is assumed that all edges are subjected to clamped boundary conditions. The panel dimensions are chosen as l_x=477 mm and l_y=381 mm. This replicates the inner dimensions of the test frame used in the experimental studies described in Section 6. The natural frequencies and modeshapes of the panels are derived using the expressions given in Refs. [21,22]. The mobilities required in Section 2 are then calculated using a modal summation.

The honeycomb test panel, shown in Fig. 2(b), comprises two face plates which are made from three plies of carbon reinforced resin. The faceplates are bound to the core honeycomb structure, which is made from fibreglass-reinforced phenolic honeycomb with a cell size of 3/8 in ($\approx$9.5 mm). The honeycomb panel has a similar mass per unit area to the aluminium test panel but a much higher static stiffness.

For practical sandwich panels the transverse dynamic stiffness is often anisotropic with respect to the x- and y-axes [23]. The most sensitive structural parameters for an accurate modelling are the out-of-plane shear modulus of the sandwich core G_x and G_y [24]. The frequency dependent transverse stiffness of the honeycomb sandwich panel is therefore modelled independently in the x- and y-directions.

The dynamic response in each axis is modelled using a basic theory [11] which considers pure bending of the cross-section and faceplates and pure transverse shear of the core. The relationship between the transverse wavenumber k and the wavenumbers corresponding to pure bending and to pure shear of a sandwich panel is given by

$$1 + \left(\frac{k_s}{k_b}\right)^2 \left(\frac{k}{k_b}\right)^2 - \left(\frac{k}{k_b}\right)^4 - \left(\frac{k_b}{k_{bf}}\right)^4 \left(\frac{k_s}{k_b}\right)^2 \left(\frac{k}{k_b}\right)^6 = 0, \tag{9}$$

where k_s is the shear wavenumber in the absence of transverse bending forces, k_b is the overall cross-section bending wavenumber in the absence of shear distortion and k_{bf} is the bending wavenumber for faceplate bending alone. These

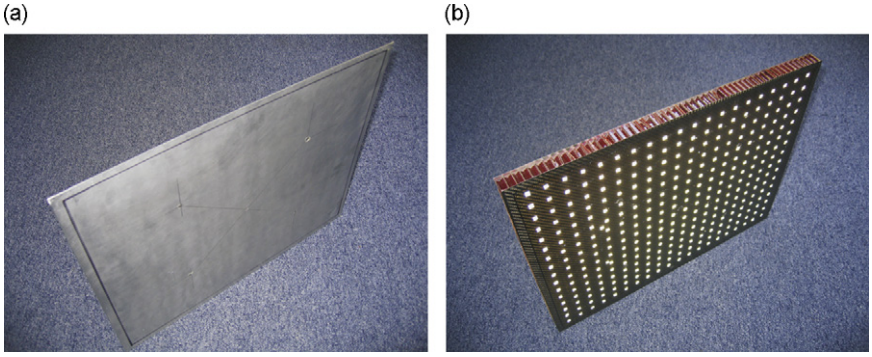

Fig. 2. Thin homogeneous aluminium test panel (a) and stiff lightweight honeycomb sandwich test panel (b).

Table 1
Geometry and physical parameters of the aluminium test panel.

Parameter	Symbol	Value	Unit
x-dimension	l_x	477	mm
y-dimension	l_y	381	mm
Thickness	h	1.6	mm
Mass density	ρ	2700	$\mathrm{kg^{-3}}$
Young's modulus	E	70	GPa
Poisson's ratio	ν	0.33	–
Damping loss factor	η	0.02	–

wavenumbers are given as

$$k_s^2 = \frac{m''\omega^2}{Gd}, \quad k_b^4 = \frac{m''\omega^2}{D_1}, \quad k_{bf}^4 = \frac{m''\omega^2}{2D_2}, \tag{10}$$

where m'' is the total panel mass per unit area, G is the transverse core shear modulus, and d is the distance between the faceplate neutral axes, which, assuming that d is much larger than the thickness of the faceplates h_f, is also used to represent the core thickness. Also D_1 is the bending stiffness of the cross-section and D_2 is the bending stiffness of an individual faceplate, which are given by

$$D_1 = \frac{Ed^2h_f}{2(1-\nu_f^2)}, \quad D_2 = \frac{Eh_f^3}{12(1-\nu_f^2)}. \tag{11}$$

where $h_f \ll d$ is the faceplate thickness. Eq. (9) has one real and two imaginary pairs of solutions. For simplicity the modeshapes of the sandwich panel in the x- and y-directions are assumed to be those of a corresponding thin homogeneous beam. The anisotropic behaviour of the honeycomb panel is modelled using a formulation given by Blevins [25], where the natural frequencies are given by

$$\omega_{m,n} = \frac{\pi^2}{\sqrt{m''}}\sqrt{D_x\left(\frac{G_m}{l_x}\right)^4 + D_y\left(\frac{G_n}{l_y}\right)^4 + \frac{2J_mJ_n + 2\nu(H_mH_n - J_mJ_n)}{(l_xl_y)^2}\alpha\sqrt{D_xD_y}}. \tag{12}$$

In the above equation, the parameters G, J and H are constants (after Warburton [21]), which depend on the mode order in x and y-directions, denoted by m and n, respectively, and the boundary conditions [21,22]. The parameters G_m and G_n should not be confused with the shear moduli G_x and G_y. Note that for simplicity the value for ν in Eq. (12) is set to zero; the parameters H_m and H_n are therefore not considered in the model. The equivalent flexural rigidities D_x and D_y in Eq. (12) are derived from the relationship $D = (\omega^2 m'')/k^4$, where k is given by the relationship in Eq. (9). Therefore D_x and D_y are frequency-dependent and need to be evaluated at $\omega = \omega_{m,n}$. In this study a Regular-Falsi root search algorithm [26] has been used to calculate the honeycomb panel natural frequencies from Eq. (12).

The model parameters given in Table 2 have been estimated with reference to dynamic response measurements on the honeycomb test panel under free support conditions. The parameter α has been adjusted to give good agreement between predicted and measured natural frequency for the [rocking, rocking] mode of the freely suspended panel [23]. Good agreement between measured and simulated structural response was achieved in the observed frequency range up to 5000 Hz [27]. For the simulation studies the mode shapes in the x-and y-directions are considered to be those of an equivalent thin homogeneous beam with pinned boundary conditions, which gave the best agreement with the measured responses of the honeycomb panel mounted in the test frame used in the experimental studies.

Fig. 3 shows the propagating bending wavenumbers of the aluminium panel and the propagating transverse wavenumbers of the honeycomb panel in the x- and y-direction. The circles and squares indicate the predicted natural frequencies of the panels (note that these do not show the components of the wavenumber in the corresponding modeshapes, but rather the values of k_x where k_y=0 and vice versa). The acoustic wavenumber in air is shown for comparison.

At low frequencies the wavenumbers of the honeycomb panel are dominated by the high bending stiffness of the sandwich cross-section and are hence much lower than those of the aluminium panel. At frequencies above 1000 Hz the

Table 2
Cross-section geometry and physical parameters for the honeycomb sandwich test panel.

Parameter	Symbol	Value	Unit
x-dimension	l_x	477	mm
y-dimension	l_y	381	mm
Thickness of face plate	h_f	0.86	mm
Core depth	d	23.09	mm
Mass density face plates	ρ_f	1250	$\mathrm{kg\,m^{-3}}$
Mass density core	ρ_c	96	$\mathrm{kg\,m^{-3}}$
Panel mass per unit area[a]	m''	4.28	$\mathrm{kg\,m^{-2}}$
Young's modulus face-plates x-axis	E_x	48	GPa
Young's modulus face-plates y-axis	E_y	43	GPa
Shear modulus core x-axis	G_x	82	MPa
Shear modulus core y-axis	G_y	155	MPa
Poisson's ratio face plates	ν_f	0.33	–
Poisson's ratio sandwich plate	ν	0	–
Damping loss factor	η	0.015	–
Anisotropic factor	α	0.035	–

[a] $m'' = 2h_f\rho_f + (d-h_f)\rho_c$.

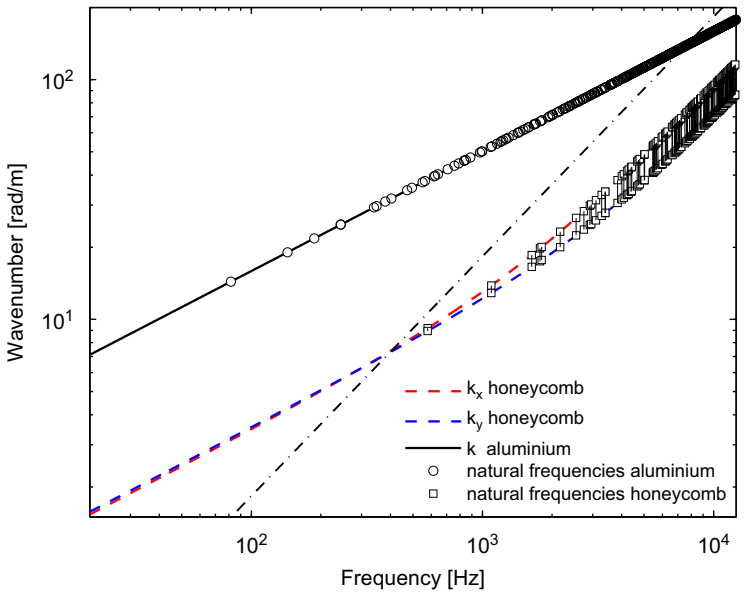

Fig. 3. Predicted dispersion curves of the propagating transverse wavenumber and resonant frequencies of the aluminium and honeycomb test panels (see legend in graph), acoustic wavenumber in air (*faint-dash-dotted*).

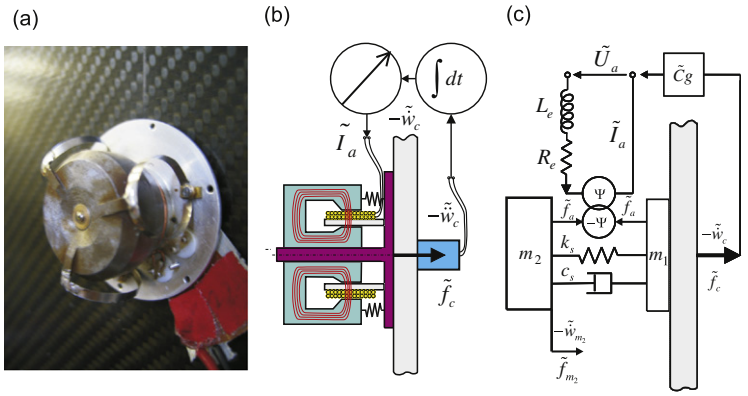

Fig. 4. (a) Actuator unit mounted on panel, (b) control unit schematics and (c) five channel feedback controller.

transverse stiffness of the honeycomb panel is increasingly shear-controlled and the wavenumber at high frequencies converges towards $k_s = \omega(m''/Gd)^{1/2}$ [11].

The acoustic critical frequency, where the acoustic wavelength equals the transverse wavelength of the panels, occurs at 7544 Hz for the aluminium panel and at 400 Hz for the honeycomb panel. The fundamental resonance of the clamped aluminium panel occurs at 82 Hz, thus well below the acoustic critical frequency. Therefore there are many structural modes which do not radiate sound efficiently and which are also not efficiently excited by acoustic fields [11]. The fundamental resonance frequency of the honeycomb panel is 579 Hz and hence above the acoustic critical frequency. Thus all structural modes of the honeycomb panel are efficient radiators of sound and are also efficiently excited by acoustic fields.

4. The control units

Fig. 4 shows the control units and the equivalent lumped parameter model considered in the simulation and experimental studies. As schematically shown in Fig. 4(b) each control unit comprises a proof-mass electrodynamic-actuator and accelerometer pair with a controller, composed of a time-integrator and amplifier electronic circuits. The inertial actuation mechanism is obtained by fixing the coil assembly to the base of the control unit where the permanent magnet is mounted via three soft circular springs and acts as a proof-mass [13,14]. For frequencies above the fundamental resonance frequency of the suspended proof-mass ($f_{\text{res}} \approx (1/2\pi)\sqrt{k_s/m_2} = 23.2$ Hz) for a current driving signal the actuator

Table 3
Parameters for control actuator model.

Parameter	Symbol	Value	Units
Base mass	m_1	13	g
Proof mass	m_2	24	g
Suspension stiffness	k_s	511	Nm^{-1}
Suspension damping coefficient	c_s	1.99	Nsm^{-1}
Voice coil coefficient	Ψ	2.16	NA^{-1}
Fundamental natural frequency	$\omega_a/(2\pi)$	23.2	Hz
Damping ratio	ζ_a	0.284	

produces a frequency independent force on the structure where it is mounted. Therefore this type of actuator can be used as a 'sky-hook' force actuator provided its fundamental resonance frequency is well below that of the structure under control [11].

In contrast to previous work [16,29], in this study the feedback response of each control unit is modelled in terms of its open- and closed-loop base impedance that it exerts to the panels where it is mounted. Considering the lumped parameter model depicted in Fig. 4c), the closed-loop base impedance of a control unit with current-driven electrodynamic proof-mass actuator is given by [27]

$$\tilde{Z}_{c_l} = \left(\tilde{Z}_s + \tilde{Z}_{m_1} - \frac{\tilde{Z}_s^2}{\tilde{Z}_{m_2}+\tilde{Z}_s}\right) + g\tilde{C}\Psi\left(1 - \frac{\tilde{Z}_s}{\tilde{Z}_{m_2}+\tilde{Z}_s}\right), \tag{13}$$

where g is the feedback gain, $\tilde{C}$ is the gain-normalised controller FRF, and Ψ is the voice coil coefficient. Also $\tilde{Z}_s = c_s + k_s/(\mathrm{j}\omega)$, $\tilde{Z}_{m_1} = \mathrm{j}\omega m_1$ and $\tilde{Z}_{m_2} = j\omega m_2$ are the actuator suspension, base mass and proof mass impedances.

In general, a practical feedback controller does not exhibit an ideal constant transfer function $\tilde{C}$; thus it affects the resulting closed-loop base impedance of the control unit. Measurements of the transfer functions of the five control boards built for this study showed that the integrator circuit can be modelled as the combination of a second-order high pass filter for DC decoupling and a first-order low pass filter which implements integration. To replicate the measured frequency responses both filters were modelled with a corner frequency of $\omega_1/(2\pi) = 14.5$ Hz. The amplifier FRF was found to have the characteristics of a first-order band-pass filter and has been modelled with lower and upper corner frequencies of $\omega_2/(2\pi) = 5$ Hz and $\omega_3/(2\pi) = 9000$ Hz, respectively. The controller frequency response function is therefore modelled as

$$\tilde{C} = \frac{\mathrm{j}\omega}{\omega_1} \frac{-\mathrm{j}\omega^3\omega_1\omega_3}{(\mathrm{j}\omega+\omega_1)^3(\mathrm{j}\omega+\omega_2)(\mathrm{j}\omega+\omega_3)} \tag{14}$$

Note that the above equation does not contain a time integration term since the actuator is modelled in terms of its base impedance, assuming an ideal velocity error sensor rather than the accelerometer used in practice. The compensator $\tilde{C}$ is normalised to have a unit magnitude in the pass band frequency region. Measurements of the amplifier electrical output resistance indicate that, for the actuators used in this study, the controller can be assumed as an ideal current source. The model parameters of electrodynamic proof-mass actuator were estimated by running a Monte Carlo simulation to fit the predicted and measured FRFs of the actuator blocked force in order to minimise the sum of the squared errors in the frequency range between 10 and 2000 Hz [27]. The actuator parameters relevant to this study are summarised Table 3.

5. Simulation studies

The two panels are modelled using the parameters specified in Section 3, assuming that the aluminium panel is clamped on all edges and the honeycomb sandwich panel is simply supported, i.e. pinned, on all edges (these are the boundary conditions that gave the best agreement with experimental results). As shown in Fig. 5, a 20×16 element grid was chosen. This resembles the measurement grid used for the laser vibrometer scans carried out in the experimental studies presented in Section 6. This grid density satisfies a spatial resolution of at least two elements per transverse wavelength on the panels at the highest frequency of interest, which is 6400 Hz. Simulations with a higher element resolution have shown that the chosen grid yields reliable results with a negligible overestimation of the spectra at the upper end of the observed frequency range.

In this study, modes with natural frequencies up to five times the observed frequency range were considered in the modal expressions for the mobility functions used in Section 2 to model the response of the panels. More specifically, modes with natural frequencies up to twice the observed frequency range (up to 12.8 kHz) were considered as 'dynamic' modes with their modal stiffness, damping and mass terms whereas modes with natural frequencies between twice and five times the highest observed frequency (between 12.8 and 32 kHz) were considered as 'residual' modes with their frequency independent stiffness and damping modal terms only [17]. For the aluminium panel a total of 1097 modes were included in the model, 427 dynamic and 670 residual. For the honeycomb panel a total of 955 modes were included in the model, 165 dynamic and 790 residual.

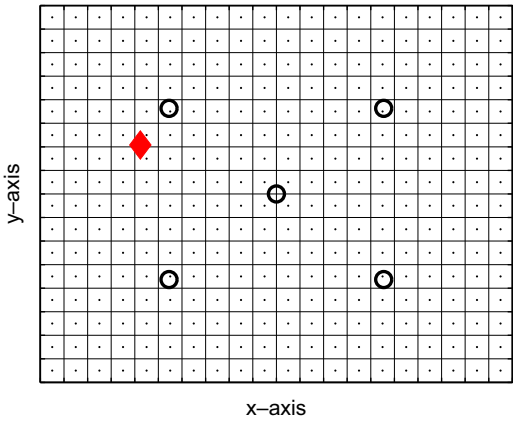

Fig. 5. Sketch of panel with element grid, control points (*circles*) and primary excitation location (*diamond*).

Table 4
Control point (CP) coordinates and primary excitation (PE) location on the test panels.

	PE	CP1	CP2	CP3	CP4	CP5
x (mm)	101	347	347	130	130	238.5
y (mm)	240	277	104	104	277	190.5

As shown in Fig. 5, one of the five control loops is placed in the centre of the panel while the other four are arranged symmetrically on the panel diagonals. The exact locations of the control loops and the position of the primary point force excitation are shown in Fig. 5 and specified in Table 4. The control loops are implemented in terms of the open- or closed-loop base impedances of the control units as given in Eq. (13). In this study a uniform set of feedback gains is considered, i.e. the same gain is applied to all five feedback loops.

5.1. Stability analysis

The stability analysis has been carried out in two phases. First the stability of each control unit in isolation has been considered using the classic Nyquist stability criterion. Second the stability of the whole set of five decentralised control units has been studied with reference to the generalised Nyquist stability criterion. In this way it has been possible to identify and discuss the intrinsic stability issues of the sensor-controller-actuator system used in each unit and the stability problems caused by the mutual interaction between the five control units.

5.1.1. Stability of each control loop

In order to analyse the stability of each control unit independently from the others, the sensor-actuator open-loop frequency response functions (OL-FRFs) of the feedback loops are calculated in the frequency range between 10 and 25 600 Hz. For this analysis the number of modes considered in the modal expressions for the panel mobility functions has been increased in accordance with the increase of the observed frequency range such that modes up to 51.2 kHz are included with their modal stiffness, damping and mass terms. The OL-FRFs for the control units with current-driven actuator and unit feedback gain are given by [27]

$$\tilde{H}_{ii} = \frac{\tilde{Y}_{c_{ii}} \tilde{C} \Psi \left(1 - \frac{\tilde{Z}_s}{\tilde{Z}_{m_2} + \tilde{Z}_s}\right)}{1 + \tilde{Y}_{c_{ii}} \left(\tilde{Z}_s + \tilde{Z}_{m_1} - \frac{\tilde{Z}_s^2}{\tilde{Z}_{m_2} + \tilde{Z}_s}\right)}, \tag{15}$$

where $\tilde{Y}_{c_{ii}}$ is the point mobility of the panel at the ith control position.

Fig. 6 shows the Bode and the Nyquist plots of the OL-FRFs $\tilde{H}_{11}$ to $\tilde{H}_{55}$ for the current controlled feedback control loops on the aluminium panel. Only two curves are visible in each plot; that for control position 5 in the centre of the panel, which gives the highest response below and around the panel fundamental resonance and that for the control positions 1, 2, 3 and 4 which are located symmetrically with respect to the axis of the panel, and therefore yield identical simulation results. In the Nyquist plot the solid lines mark the frequency response between 0 and 100 Hz which contains both the actuator and the panel fundamental resonance frequency, while the faint lines mark the frequency response from 100 Hz to 25.6 kHz. The presence of circles in the left half-plane of the Nyquist plot indicates that the control loops are only conditionally stable. The gain margins for the control loops are limited by the 180° phase shift of the OL-FRFs, which is due

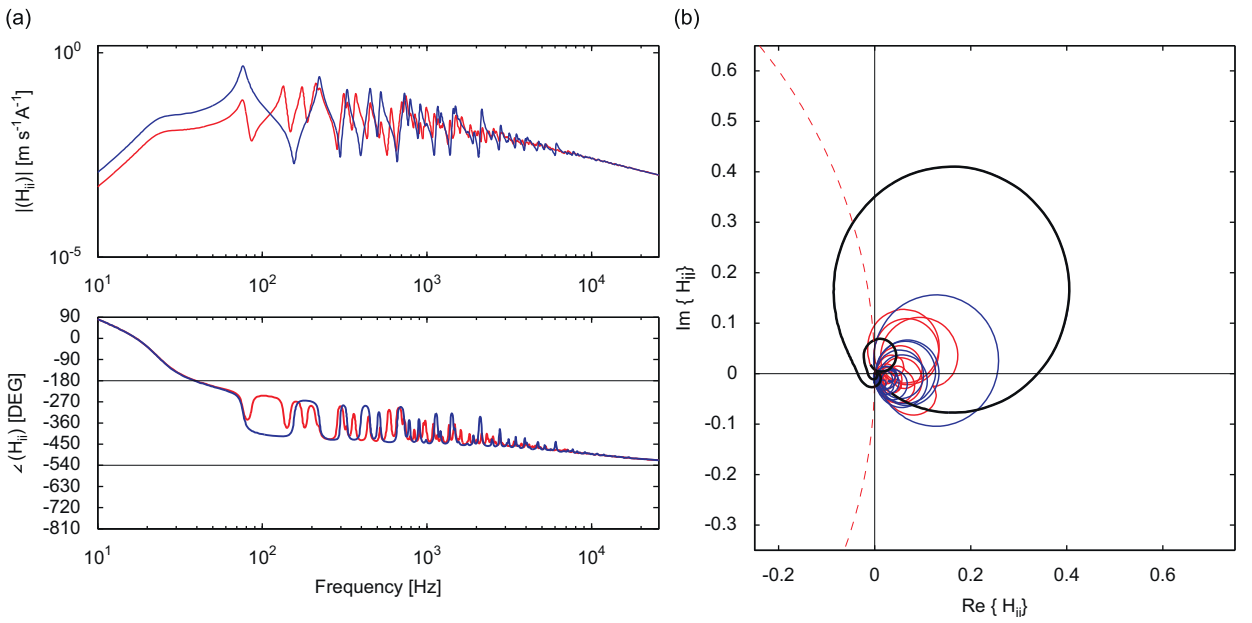

Fig. 6. Simulated OL-FRFs of the current-controlled feedback loops on the aluminium panel. Thick solid lines in the Nyquist plot mark the FRFs in the frequency range from 0 to 100 Hz and the (*dashed*) line marks the unit circle around the Nyquist stability point.

to the actuator fundamental resonance in combination with the FRF of the feedback controller. These circles indicate that, even if small control gains that guarantee stability are implemented, the parts of the OL-FRFs that fall within the unit circle around the Nyquist stability point at $(-1,0j)$ result in an enhancement of the structural response in that frequency band [18]. For frequencies above the actuator resonance frequency, the circles of the OL-FRFs migrate into the right half-plane of the Nyquist plot. This indicates that, for frequencies well above the fundamental resonance frequency of the actuator, the velocity feedback loops produce active damping. The magnitudes of the circles indicate how much active damping is produced for given control gain, thus how efficiently the response of the structural modes is attenuated at the corresponding resonance frequencies [16]. At very high frequencies the circles of the OL-FRFs migrate back into the left half-plane of the Nyquist plot. In this frequency range the magnitudes of the OL-FRFs are very small compared with that of the low frequency circle due to the actuator fundamental resonance; hence these parts of the OL-FRFs do not pose stability limits. Nevertheless, control spillover effects in this high frequency band occur, although they are of smaller amplitude than that around the fundamental resonance of the actuator.

Fig. 7 shows the corresponding results for the honeycomb panel. In the Nyquist plot the solid lines mark the frequency response between 0 Hz and 2 kHz and the faint line those from 2 to 25.6 kHz. The results show the same 180° phase shift around the actuator fundamental resonance frequency and the resulting low frequency circle in the left half-plane of the Nyquist plot. However, compared with the results in Fig. 6, in this frequency range the magnitudes of the OL-FRFs of the feedback loops on the honeycomb panel are very low and hence allow higher gain margins. This is because the first resonance frequency of the sandwich panel is much higher than the actuator fundamental resonance. For the aluminium panel the maximal stable gain for current-controlled feedback loops is 28 while that for the feedback loops on the honeycomb panel is 2134.

5.1.2. *Stability of the five control loops*

As discussed by González Díaz et al. [28,29] and Baumann and Elliott [30], the stable gain margin for a feedback control system with multiple proof-mass electrodynamic actuators reduces with increasing number of feedback loops. This is due to cross-talk, i.e. cross excitation effects between the control units. Hence, to assess the stability of the control system with five decentralised control loops, it is necessary to evaluate the eigenvalues of the fully populated $[5\times5]$ matrix $\mathbf{\tilde{H}}$ of OL-FRFs between the output of the five control sensors and the actuator input signals, where the elements for the OL-FRFs matrices $\mathbf{\tilde{H}}$ are given by Eq. (15). According to the generalised Nyquist stability criterion [18], to guarantee stability, the locus of the eigenvalues must not encircle the instability point $(-,j0)$. Figs. 8 and 9 show the Bode diagram and the locus plots with the eigenvalues of the fully populated OL-FRF matrices for the control system installed on the aluminium and honeycomb panel. In contrast to the plots of the OL-FRF in Figs. 6 and 7, the locus of the eigenvalue plots exhibit five curves, each representing one of the system eigenvalue functions. The results exhibit similar characteristics to the OL-FRFs for the individual feedback loops. However, the loops are slightly expanded, which results in a decrease in the stable gain margin. The system stability is limited by the locus of the eigenvalue that forms the largest circle crossing the negative real axis in the Nyquist plot. The maximum gain for the control system installed on the aluminium panel is reduced by 28.5

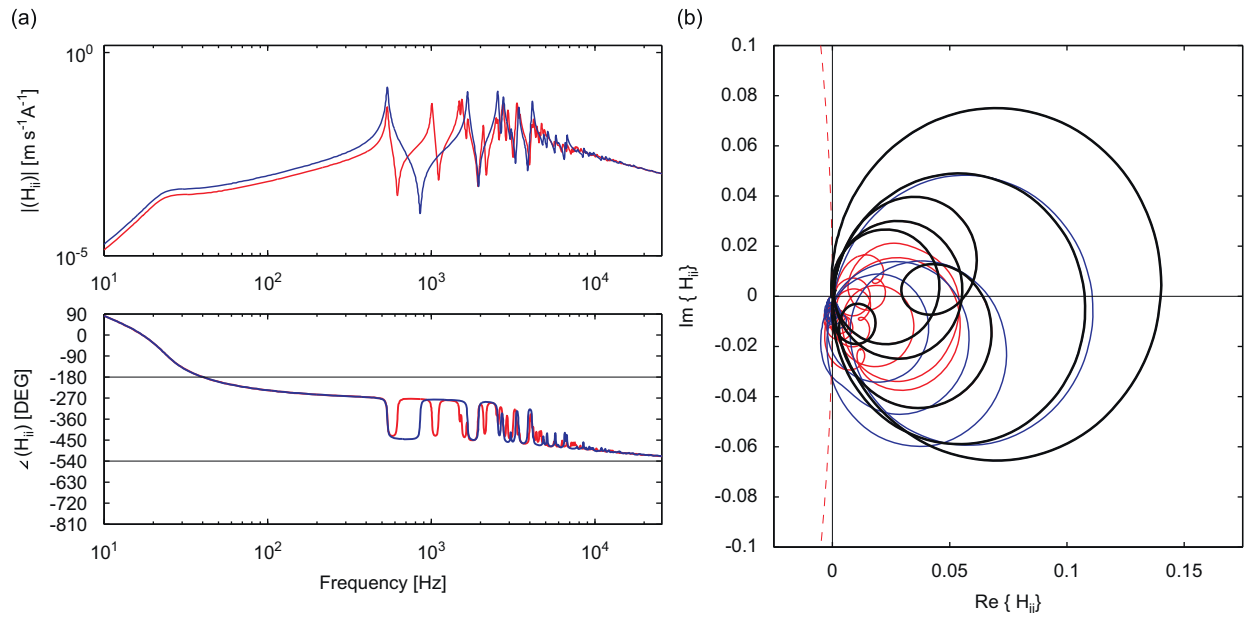

Fig. 7. Simulated OL-FRFs of the current-controlled feedback loops on the honeycomb panel. Thick solid lines in the Nyquist plot mark the FRFs in the frequency range from 0 to 2000 Hz and the (*dashed*) line marks the unit circle around the Nyquist stability point.

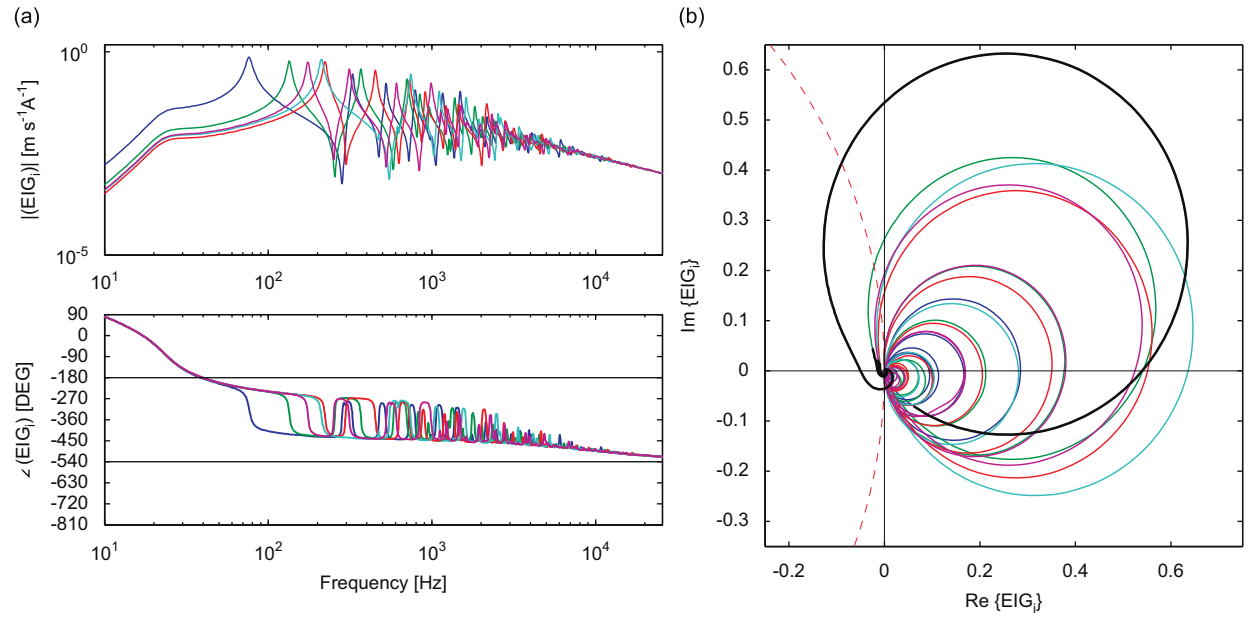

Fig. 8. Simulated eigenvalues of the OL-FRFs of the control system with current-controlled feedback loops on the aluminium panel. Thick solid lines in the Nyquist plot mark the FRFs in the frequency range from 0 to 100 Hz and the (*dashed*) line marks the unit circle around the Nyquist stability point.

percent to 20, while for the control system installed on the honeycomb panel it is reduced by 42 percent to 1244, which is still much higher than that for the aluminium panel.

5.2. Control performance

The performance of the control system with five decentralised control units operating is assessed for the cases where the panels are excited by a point force and a plane acoustic wave with angles of incidence $\theta = 45^\circ$ and $\varphi = 45^\circ$. The response of the panels is calculated using Eq. (1). The panels' kinetic energy and total sound power radiated are then calculated using Eqs. (6) and (7), respectively.

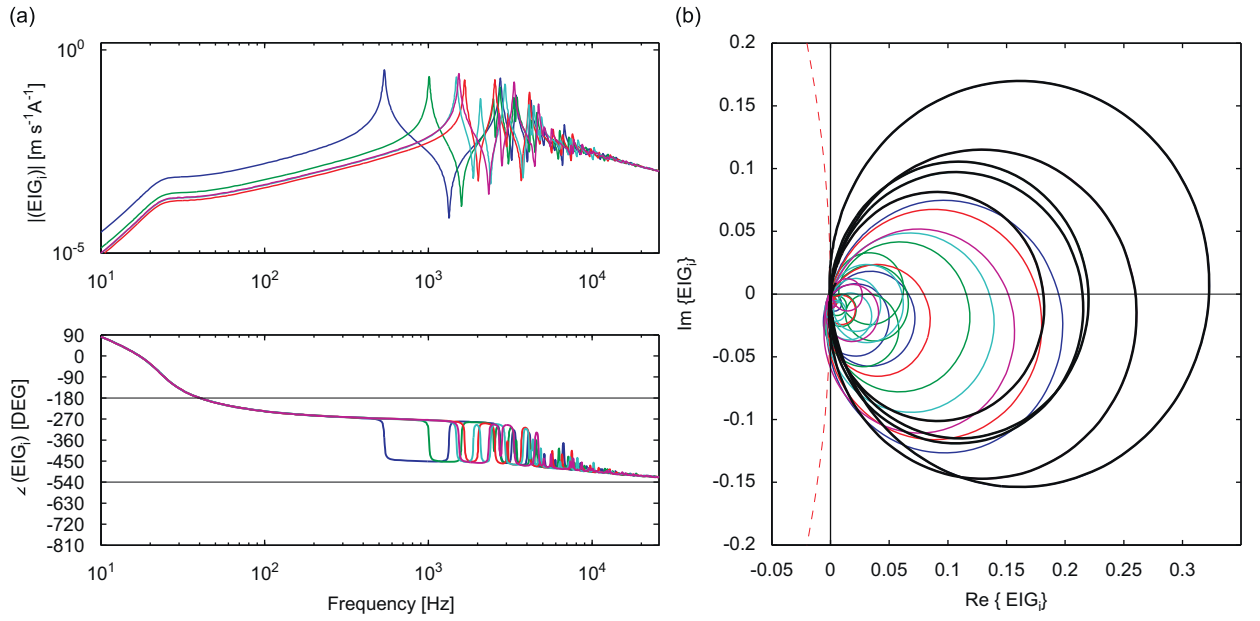

Fig. 9. Simulated eigenvalues of the OL-FRFs of the control system with current-controlled feedback loops on the honeycomb panel. Thick solid lines in the Nyquist plot mark the FRFs in the frequency range from 0 to 2000 Hz and the (*dashed*) line marks the unit circle around the Nyquist stability point.

5.2.1. Point force excitation

Fig. 10 shows the predicted spectra of the panel kinetic energy and radiated sound power for the aluminium panel (left hand side) and the honeycomb panel (right hand side) excited by a point force. The kinetic energy spectra of the panels without control units, shown in Figs. 10(a) and (b), are characterised by a set of well separated and sharp resonance peaks of low order modes of the panels; those of the aluminium panel occur between the fundamental resonance at 82 Hz and about 500 Hz, while those of the honeycomb panel occur between the fundamental resonance at 579 Hz and about 2000 Hz. Above these two frequency bands, the kinetic energies of the two panels are characterised by smoother spectra. This is because, with plate structures, the number of modes significantly excited at any one frequency, i.e. the modal overlap factor, increases with frequency [11]. The spectrum of the honeycomb panel kinetic energy shows a dip between 3000 and 3800 Hz, which is due to the location of the primary force and also due to the uneven frequency distribution of resonance frequencies of the anisotropic honeycomb panel. For frequencies below 4000 Hz the kinetic energy of the plain aluminium panel is much higher than that of the plain honeycomb panel. Above 4000 Hz the responses of aluminium and honeycomb panel are of comparable level.

Considering next the sound radiation from the two panels without control units shown in Figs. 10(c) and (d), in contrast to the result for the kinetic energy, above the fundamental resonance frequency at 579 Hz, the sound radiation levels for the honeycomb panel are slightly higher than those for the aluminium panel. This is due to the fact that, as discussed in Section 3, the two panels have significantly different structural response and sound radiation properties at low and mid audio frequencies. The aluminium panel is characterised by many resonant modes at low and mid audio frequencies (the fundamental resonance is at 82 Hz) which, however, poorly radiate sound below the acoustic coincidence frequency at 7544 Hz. In contrast the honeycomb panel is characterised by comparatively fewer modes at low and mid audio frequencies (the fundamental resonance is at 579 Hz), which on the other hand efficiently radiate sound since they all resonate above the acoustic coincidence frequency at around 400 Hz.

Fig. 10 also shows the predicted responses and sound radiation spectra of the two panels with open- and closed-loop control units. The mass effect of the open-loop control units lowers the resonance frequencies of the low order modes of the panels. Also, passive damping effects of the open-loop control units reduce the amplitude of the resonance peaks over a wide frequency band. The amplitudes of low order resonances are reduced by up to 15 dB for the aluminium panel and up to 7 dB for the honeycomb panel. These damping effects are primarily due to the relative motion between the base and suspended mass of the actuator which produces (a) structural loss in the suspension springs, (b) viscous loss in the gap between the magnet and the coil, (c) friction damping between the magnet and the guiding stinger and (d) electrical dissipation due to Eddy currents induced by the magnet on the components of the actuator.

For the aluminium panel, when the feedback loops are closed with progressively higher control gains, 10–15 dB additional reductions of both kinetic energy and radiated sound power are predicted in the frequency range from 50 to 300 Hz. As the feedback gains are increased the panel response and radiated sound power are enhanced in the frequency region between 30 and 50 Hz. This is because, around the actuator fundamental resonance frequency, the control units

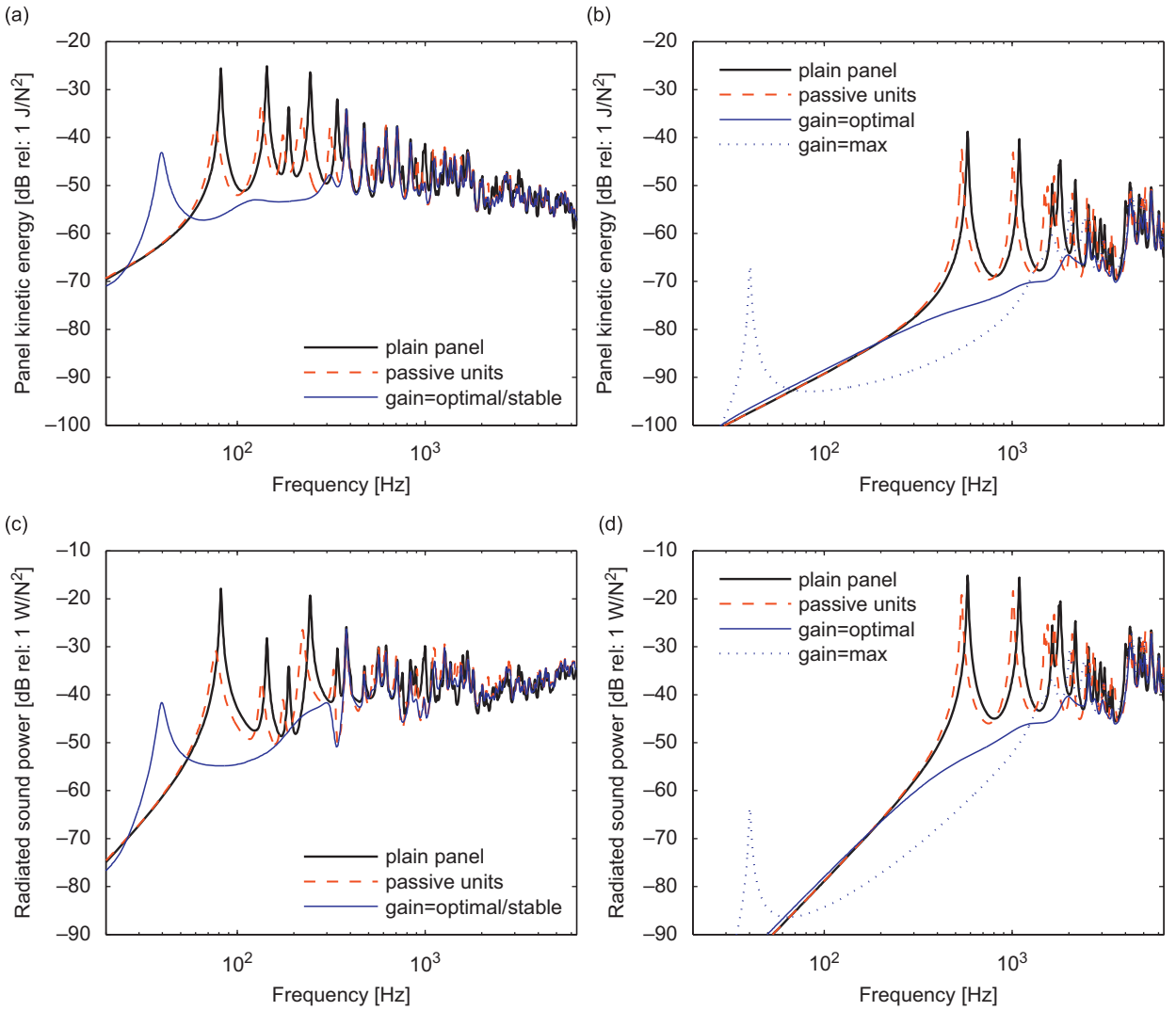

Fig. 10. Predicted panel kinetic energies (*top plots*) and radiated sound powers (*bottom plots*) for point force excitation. Aluminium panel left hand side, honeycomb panel right hand side; panel kinetic energy top row, radiated sound power bottom row.

generate negative damping and thus input power into the structure rather than absorbing it from the structure. This phenomenon is normally reported as control spillover.

For the honeycomb panel, when the feedback loops are closed with progressively higher control gains, 20–30 dB additional reductions of both kinetic energy and radiated sound power are predicted in the frequency range from 400 to 2000 Hz. Below 400 Hz the honeycomb panel response is stiffness-controlled and drops rapidly with decreasing frequency. As a result, there is nearly no low frequency control spillover produced by the actuators.

The results plotted in Fig. 11 and summarised in Table 5 provide an overview of the passive and active response and sound radiation properties of the two panels when they are excited by a point force. The results presented are the averaged levels in the frequency range between 5 and 2244 Hz which includes the upper end of the 1/3 octave band with centre frequency 2000 Hz. As can be seen from Fig. 10, above this frequency range the control units do not produce significant reductions on either of the two panels.

The two graphs in Fig. 11 show that in absence of the control units the aluminium panel is characterised by 10.8 dB higher kinetic energy and 5.5 dB lower radiated sound power than the honeycomb panel. As discussed above, this is the result of the different behaviour of the two panels in terms of structural response and sound radiation, which can be brought back to the values of the fundamental natural frequency and the acoustic coincidence frequency of the two panels as reported in Table 5.

When the five control units are fixed on the two panels, both the kinetic energy and radiated sound power diminish by about 0.5–2.5 dB. When the five control loops are closed with increasing control gains, the kinetic energy and radiated

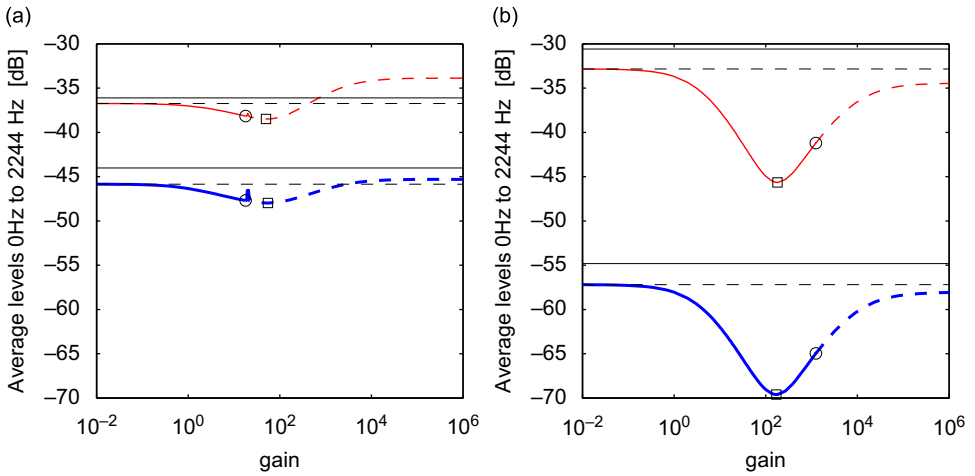

Fig. 11. Frequency averaged (5–2244 Hz) panel kinetic energy and radiated sound power for point force excitation; (a) aluminium panel and (b) honeycomb panel. Panel kinetic energy (*solid-blue*) and radiated sound power (*faint-red*). Gain of highest reductions (*squares*) and maximal stable gain (*circles*). The horizontal lines mark the frequency averaged levels for the panels without control units (*faint*) and for open-loop control units mounted to the panels (*faint-dashed*). (For interpretation of the references to colour in this figure legend, the reader is referred to the web version of this article.)

Table 5
Overview of the passive and active response and sound radiation properties of the aluminium and the honeycomb panels when they are excited by a point force or by an acoustic plane wave.

	Point force excitation		**Acoustic plane wave excitation**	
	Aluminium panel	**Honeycomb panel**	**Aluminium panel**	**Honeycomb panel**
Fundamental natural frequency actuators	23.2	23.2	23.2	23.2
Maximum stable gain 1 feedback loop	28	2134	28	2134
Maximum stable gain 5 feedback loops	20	1244	20	1244
Panel fundamental natural frequency (Hz)	82	579	82	579
Panel acoustic critical frequency (Hz)	7544	400	7544	400
		Gain settings with respect to panel kinetic energy		
Optimum gain 5 feedback loops	55	171	45	285
Optimum/stable gain 5 feedback loops	18		14	
		Freq. averaged kinetic energy (dB)		
Plain panel	−44.0	−54.8	−65.7	−72.8
Panel with open loop control units (dB)	−45.8	−57.2	−71.5	−74.8
Optimum gain implemented	−48.0	−69.6	−79.4	−90.8
Optimum/stable gain implemented	−47.7		−77.4	
		Gain settings with respect to radiated sound power		
Optimum gain 5 feedback loops	50	180	26	285
Optimum/stable gain 5 feedback loops	18		14	
		Freq. averaged radiated sound power (dB)		
Plain panel	−36.1	−30.6	−57.3	−48.9
Panel with open loop control units	−36.7	−32.8	−61.7	−50.9
Optimum gain implemented	−38.5	−45.6	−65.0	−66.8
Optimum/stable gain implemented	−38.2		−64.9	

sound power vary with a typical performance curve, which is characterised by a single optimum control gain as specified by the square symbol. Thus, as summarised in Table 5, when the control gain of the five feedback loops on the aluminium panel are set to values around 50 and 55, compared to the plain panel, the overall reductions of the kinetic energy and radiated sound power are 4 and 2.4 dB, respectively. However Fig. 11(a) indicates that the optimal feedback gains exceed the stability limit of the five control units, which, as highlighted by the circles and summarised in Table 5, are set to a value of 18. Thus, when the optimal/stable gains are implemented, compared to the plain panel, the overall reductions of the kinetic energy and radiated sound power are 3.7 and 2.1 dB, respectively. Similarly, as indicated in Table 5, when the control gain of the feedback loops in the honeycomb panel are set to values around 171 and 180, compared to the plain

panel, the overall reductions of the kinetic energy and radiated sound power are 14.8 and 15 dB, respectively. In this case, the optimal control gains do not exceed the stability limits, which occur at much higher values as highlighted by the circles in Fig. 11(b). As discussed in Section 5.1, the stability limit for the feedback loops is determined by the ratio between the fundamental natural frequency of the panel and the fundamental natural frequency of the actuators, which, as summarised in Table 5, is much higher for the honeycomb panel.

In summary it can be concluded that, for a point force excitation, the plain honeycomb panel is characterised by a lower response than the plain aluminium panel but higher radiated sound power. However, when the five control units are implemented with the optimal/stable feedback gains, much larger reductions of both kinetic energy and radiated sound power are obtained on the honeycomb panel so that, overall, with respect to the aluminium panel, the honeycomb panel is characterised by a 21.9 dB lower response and a 7.4 dB lower radiated sound power. It is interesting to note that these control effects on the honeycomb panel are obtained with about 10 times higher control gains than those on the aluminium panel, which, however, can be implemented since, as reported in Table 5, the maximum stable gain for the honeycomb panel is much higher than that on the aluminium panel. Although the actual excitation spectra in vehicles will vary from one application to another, this gives an indication of the likely dependence of the overall benefit on control gain.

5.2.2. *Acoustic plane wave*

Considering now a plane wave excitation with $\theta = 45^{\circ}$ and $\varphi = 45^{\circ}$, Fig. 12 shows the predicted panel kinetic energy and radiated sound power for the aluminium panel (left hand side) and the honeycomb panel (right hand side). The spectra of the kinetic energy and radiated sound power of the panels without control units are similar to those shown in the corresponding plots for the point force excitation in Fig. 10. However, for the aluminium panel the spectra are

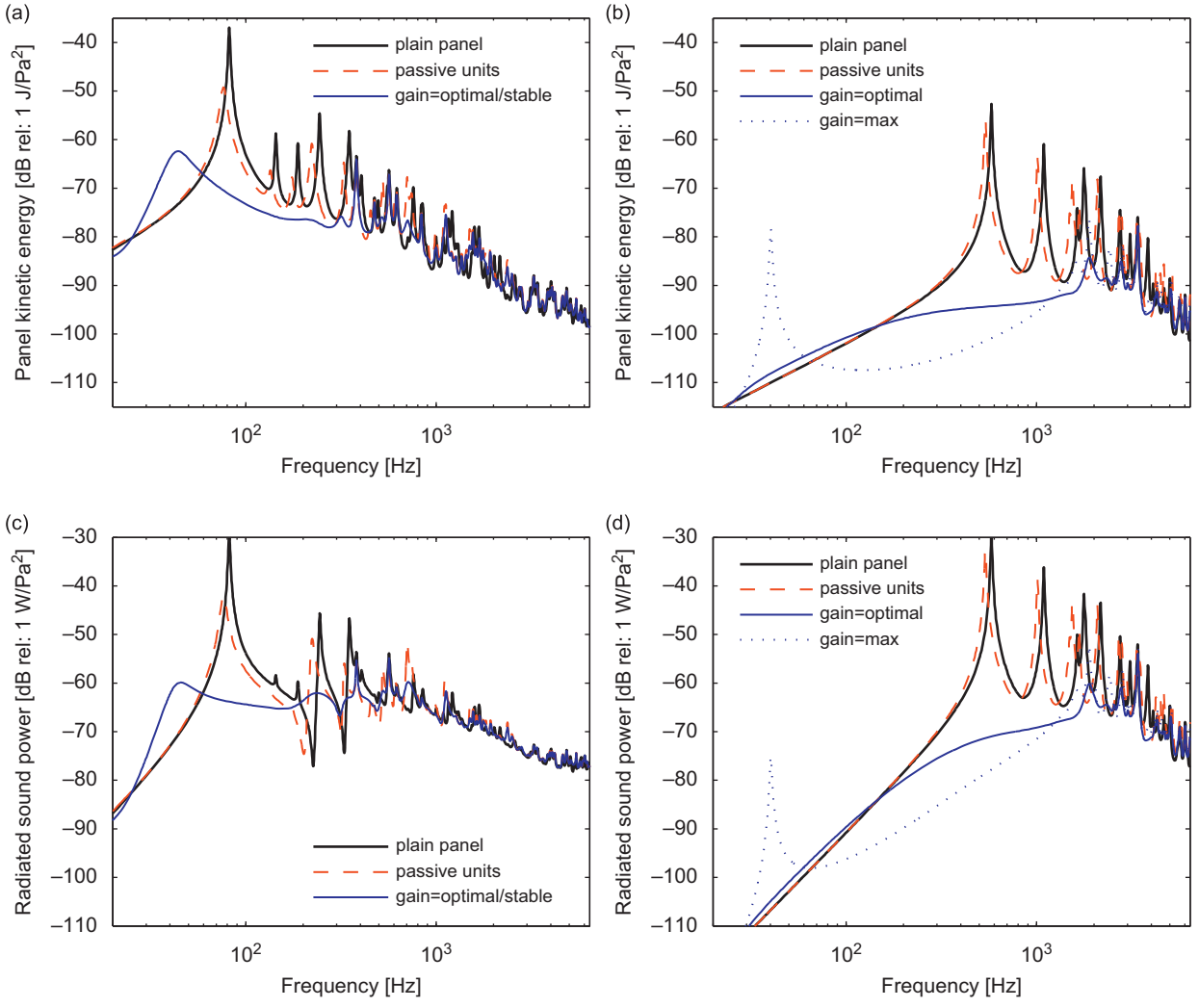

Fig. 12. Predicted panel kinetic energies (*top plots*) and radiated sound powers (*bottom plots*) for acoustic plane wave excitation. Aluminium panel left hand side, honeycomb panel right hand side; panel kinetic energy top row, radiated sound power bottom row.

characterised by a smaller number of well-separated resonance peaks. This is due to the fact that below the coincidence frequency at 7544 Hz the distributed acoustic field does not efficiently excite all low order modes of the aluminium panel. In contrast, all modes of the honeycomb panel are well excited since its 400 Hz acoustic coincidence frequency is lower than the first resonance frequency at 579 Hz. The spectra for both panels tend to roll off at a higher rate as the frequency increases. This is because the modal excitation strength of the acoustic wave tends to decrease with rising frequency. Comparing the plots in Fig. 10 and Fig. 12, it is noted that for both panels the narrow-band effects produced by the control units with open and closed feedback loops are very similar.

The passive and active response and sound radiation properties of the two panels excited by the plane acoustic wave are summarised in the two graphs in Fig. 13 and Table 5. Similarly to the results presented in Section 5.2.1, the two graphs show that the plain aluminium panel is characterised by 7.1 dB higher level of kinetic energy and 8.4 dB lower level of radiated sound power than the plain honeycomb panel. Thus, compared to the case of point force excitation, with the acoustic plane wave excitation, there are smaller differences between the kinetic energies and between the radiated sound powers of the two panels. This is due to the different behaviour of the two panels in terms of structural response and sound radiation, which discussed in Section 3 are linked to values of the fundamental natural frequency and the acoustic critical frequency of the two panels.

When the five control units are fixed on the aluminium and honeycomb panels the kinetic energy diminishes, respectively, by 5.8 and 2.0 dB and the radiated sound power diminishes, respectively, by 4.4 and 2.0 dB. Thus, with plane wave excitation, the passive effect of the control units is more marked on the aluminium panel. This is due to the fact that the structural response and radiated sound power of the aluminium panel for plane wave excitation rolls off with increasing frequency, thus the average levels are dominated by fewer low order resonant modes, which are effectively damped by the open-loop control units.

When the five control loops are closed with increasing control gains, as summarised in Table 5, if the feedback loops in the aluminium panel are set to values around 45 and 26, the overall reductions of the kinetic energy and radiated sound power compared to the plain panel, are 13.7 and 7.7 dB, respectively. Thus, when the aluminium panel is excited by an acoustic plane wave instead of a point force, much larger reductions of kinetic energy and radiated sound power are produced by the feedback loops. Nevertheless, also in this case, as shown in Fig. 11(b), the optimal feedback gains exceed the stability limit of the five control units. In this case, as highlighted by the circles and summarised in Table 5, the optimal gains are set to a value of 14 so that when they are implemented, compared to the plain panels, the overall reductions of the kinetic energy and radiated sound power are brought down slightly to 11.7 and 7.6 dB. Thus with the plane wave excitation the limits imposed on the control gain by stability have less effect on the overall performance of the feedback loops. Table 5 indicates that when the control gains of the feedback loops on the honeycomb panel are set to a value around 285, the overall reductions of the kinetic energy and radiated sound power compared to the plain panel, are 18.0

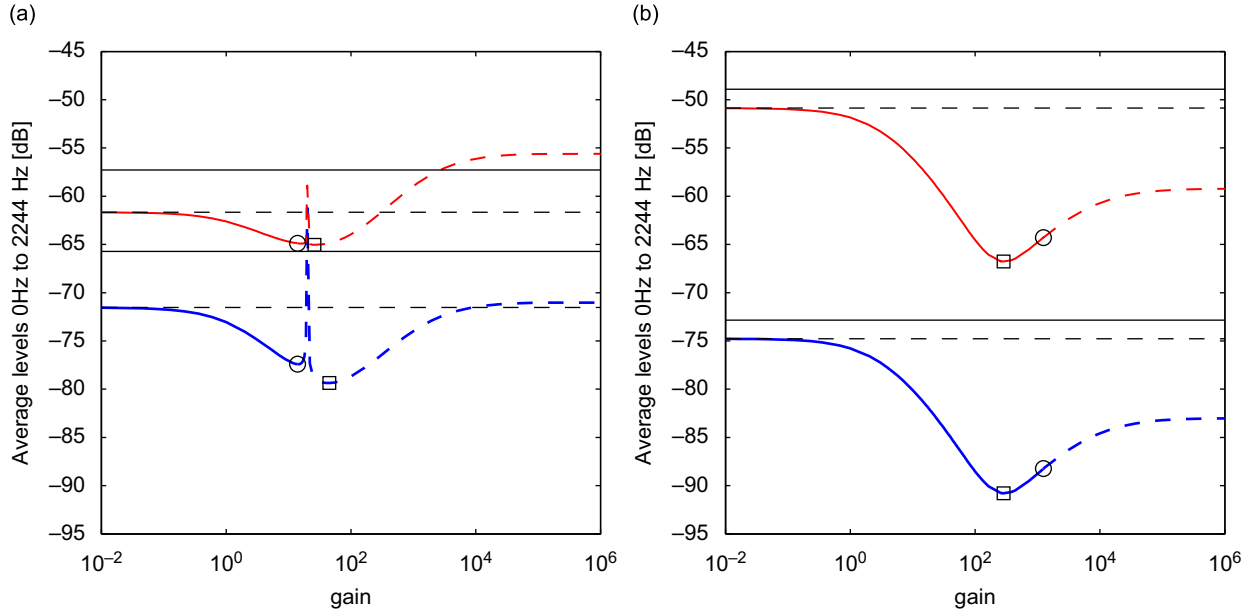

Fig. 13. Frequency averaged (5–2244 Hz) panel kinetic energy and radiated sound power for acoustic plane wave excitation; (a) aluminium panel and (b) honeycomb panel. Panel kinetic energy (*solid-blue*) and radiated sound power (*faint-red*). Gain of highest reductions (*squares*) and maximal stable gain (*circles*). The horizontal lines mark the frequency averaged levels for the plain panels (*faint*) and for open-loop control units mounted to the panels (*faint-dashed*). (For interpretation of the references to colour in this figure legend, the reader is referred to the web version of this article.)

and 17.9 dB, respectively. In this case, the optimal control gains do not exceed the stability limits, which occur at much higher values as highlighted by the circles in Fig. 13(b).

In summary, similarly to the case of point force excitation, it can be concluded that for a plane acoustic wave excitation, the plain honeycomb panel is characterised by a lower response than the plain aluminium panel but higher radiated sound power. However, when the five control units are implemented with the optimal/stable feedback gains, a 13.4 dB lower average kinetic energy level is obtained on the honeycomb panel than on the aluminium panel. With control the average radiated sound power obtained on the honeycomb panel is 1.9 dB lower than on the aluminium panel, while without control the averaged radiated sound power levels would be 8.4 dB higher than those obtained from the aluminium panel. Also in this case the control effects on the honeycomb panel are obtained with much higher control gains (about 20 times) than those on the aluminium panel, which, however, can be implemented since, as reported in Table 5, the maximum stable gain for the honeycomb panel is about 60 times greater than that on the aluminium panel.

6. Experimental studies

This section presents results of experimental studies on the control stability and control performance when the control system with five decentralised control units described in Section 4 is mounted on the aluminium and the honeycomb panel described in Section 3. For the experimental studies, the panels were mounted in a test frame and placed in the window of a sound transmission suite, as shown in Fig. 14. The resulting boundary conditions for the honeycomb panel have been found to be between pinned and clamped conditions (The measured fundamental frequency is 735 Hz, those predicted for pinned and clamped boundaries are 579 and 1184 Hz, respectively). Also, it has been found that the aluminium panel was affected by in-plane loads due to imperfect mounting conditions and panel curvature effects which shifts the measured resonance frequencies above those predicted for an ideal flat panel with clamped boundary conditions (The measured fundamental resonance frequency is 117 Hz, those predicted for pinned and clamped boundaries are 44 and 82 Hz, respectively).

The five control actuators were mounted on the source side of the panels using a thin layer of adhesive wax. The control locations are those specified in Table 4. The accelerometer sensors were mounted at the centre of the actuator footprints on the opposite side of the panels (receiving side) using a thin layer of adhesive wax. Altogether the five control units (excluding the controller) add a mass of 0.185 kg, which corresponds to a 23.5 percent increase to the 0.785 kg mass of the panels.

As shown in Fig. 14, on the source side, the panels were excited (a) mechanically using a shaker and (b) by the direct acoustic field generated by a loudspeaker placed in front of the panels at about 80 cm distance. The excitation point for the shaker is that specified in Table 4. In the case of shaker excitation the input force applied to the panel was measured and used as the reference signal for the results. For the acoustic excitation, the voltage input to the loudspeaker was measured and used as the reference signal. The effects introduced by the loudspeaker and by the source room responses have been considered by correcting the measured responses of the panel with the magnitude of the transfer function between the loudspeaker input voltage and the spatially averaged sound pressure measured in close proximity to the panel surface on the source side. Although the direct acoustic field will have a different spatial correlation than a reverberant acoustic field, at low frequencies they should be comparable. In practical applications it is more likely to encounter direct acoustic fields than reverberant fields, i.e. jet engine noise exciting a fuselage panel. The effect of different angles of incidence and different types of excitations on the sound transmission is discussed in Ref. [9].

As shown in Fig. 14(c), on the receiver side a laser vibrometer was used to measure the response of the panel on a grid of 16×20 points. The panel kinetic energy and radiated sound power are estimated from these measurements using the formulations for the 'elemental approach' described in Section 2. The panel is subdivided into a uniform grid of elements; the panel kinetic energy and radiated sound power are then estimated using Eqs. (6) and (7), respectively, with the measured velocities at the centres of the elements. The radiated sound power has also been estimated from sound pressure measurements made with nine microphones on an hemispherical grid under semi-anechoic conditions in the receiving room. The results from both measurement methods yield good agreement over the entire frequency range of interest [27]. For brevity the results from microphone measurements are not presented in this paper.

Fig. 14. Set-ups for shaker excitation (a), loudspeaker excitation (b) and laser vibrometer measurements (c).

6.1. Stability analysis

In the same way as in Section 5, the stability of the real control system has been assessed in two stages, which are discussed in the following two subsections.

6.1.1. Stability of each feedback loop

The stability of each control unit has been assessed with reference to the sensor-actuator open-loop frequency response functions (OL-FRFs) between the voltage input to the integrator of the control boards that drive the actuator and the output voltage from the signal conditioner of the corresponding sensor. The gain for each control loop is normalised to guarantee a 6 dB gain margin, i.e. it is set to half the maximum stable gain. The measured OL-FRFs for the five channels of the control system mounted on the aluminium panel and the honeycomb panel are shown in Figs. 15 and 16, respectively.

As noted in the simulation study in Section 5, the Bode diagrams in Figs. 15(a) and 16(a) for the control system installed on the aluminium and the honeycomb panel show a low frequency resonance due to the actuator dynamics and then multiple resonances due to the responses of the panels. However, these plots also show large resonance peaks and anti-resonance troughs in the frequency range between 7 and 9 kHz. Measurements on the base impedance of the control units suggest that this is due to mounting resonances of the actuator and accelerometer units [27]. For the control system on the honeycomb panel additional problems at high frequencies may occur due to resonances of the honeycomb cross-section [31].

As for the simulation study in Section 5, the gain margins for the control loops on the aluminium panel are limited by the actuator fundamental resonance, which at low frequencies produces circular loci in the left half-plane of the Nyquist plot in Fig. 15(b). For frequencies above the actuator resonance frequency, the loci of the OL-FRFs migrate into the right half-plane of the Nyquist plot and are characterised by multiple circles due to the well separated resonances of the panel. Here the velocity feedback loops reduce the structural response of the panel by means of active damping. The relatively large magnitudes of the circles in the right half-plane compared with that in the left half-plane of the Nyquist plot indicate that the response of low order structural modes of the aluminium panel are attenuated efficiently around their resonance frequencies [28]. However, in contrast to the simulation results presented in Section 5, at very high frequencies, the loci of the OL-FRFs migrate back into the left half-plane of the Nyquist plot. As discussed above, this is predominantly due to the actuator mounting resonance and also due to complex dynamics of the actuator components (i.e. circular springs) that are neglected in the actuator model. However, in this high frequency range the magnitudes of the OL-FRFs are very small compared with that of the low frequency circle due to the actuator fundamental resonance; hence these parts of the loci do not pose stability limits, but are expected to cause small control spillover effects at high frequencies.

The measured OL-FRFs of the control loops on the honeycomb panel in Fig. 16(b) show the same low frequency circle in the left half-plane and then at higher frequencies multiple resonant circles in the right half-plane of the Nyquist plot.

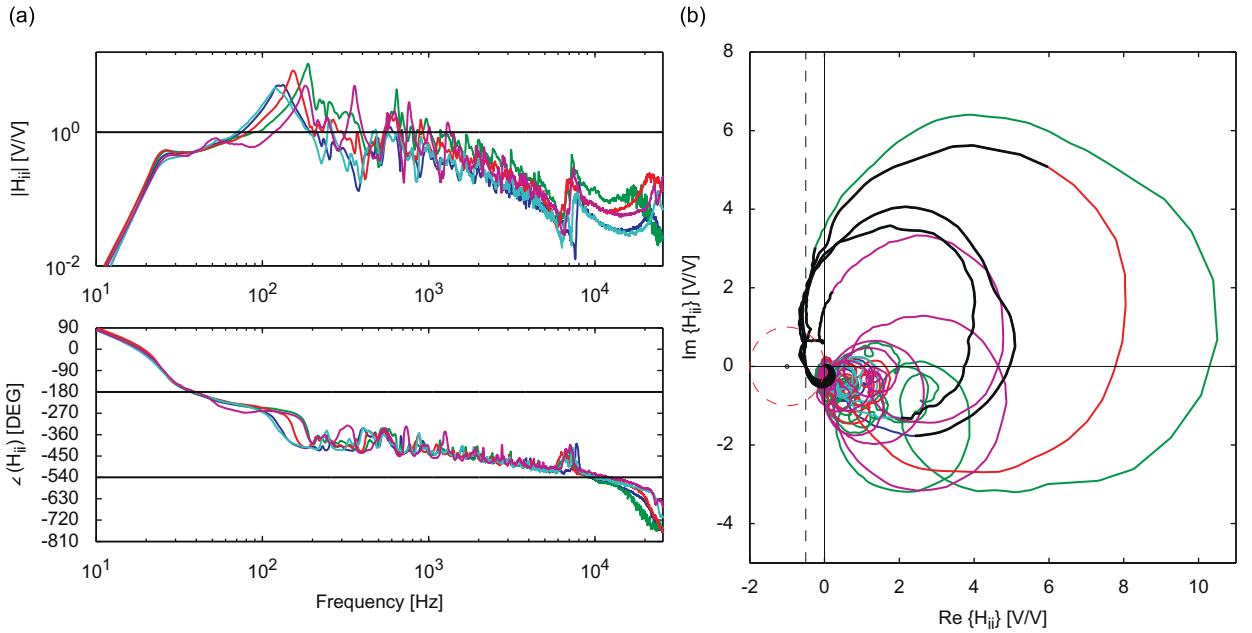

Fig. 15. Open-loop FRFs of the control units on the aluminium panel. Thick solid lines in the Nyquist plot mark the FRFs in the frequency range from 0 to 150 Hz and the (*dashed*) lines mark the 6 dB gain margin limit and the unit circle around the Nyquist stability point.

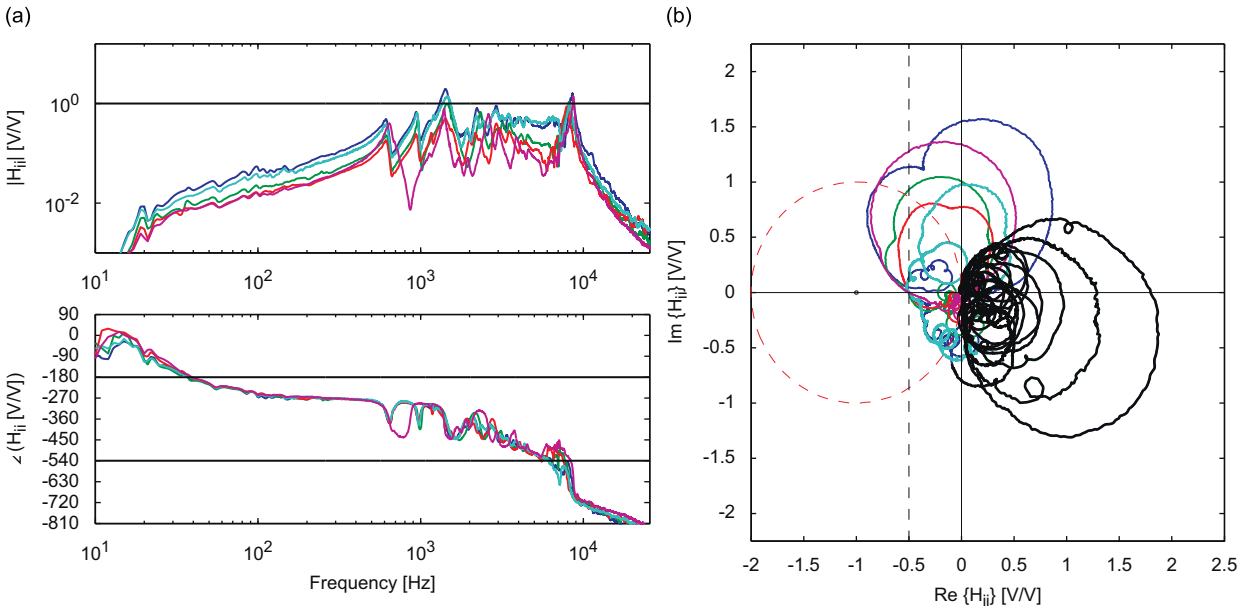

Fig. 16. Open-loop FRFs of the control units on the honeycomb panel. Thick solid lines in the Nyquist plot mark the FRFs in the frequency range from 0 to 3000 Hz and the (*dashed*) lines mark the 6 dB gain margin limit and the unit circle around the Nyquist stability point.

However, in contrast to the OL-FRFs measured on the aluminium panel shown in Fig. 15(b), the magnitudes in the low frequency range are very small and would hence allow for high gain margins. However, for frequencies above about 3000 Hz, the circles of the OL-FRFs with high magnitude migrate onto the left half-plane of the Nyquist plot. Thus higher control spillover effects occur at these high frequencies than around the fundamental resonance of the actuator. Also the maximum stable gain is limited by high amplitude circles in the left hand half-plane produced by the actuator mounting resonances, which occur in the frequency range between 7 and 9 kHz and not by the circle in the left half-plane produced by the actuator fundamental resonance.

In summary, considering the practical issues with the panel mounting conditions and therefore nonideal structural response, a good general agreement between the experimental sensor-actuator OL-FRFs in Figs. 15 and 16 and the simulation results shown in Figs. 6 and 7 is achieved. The panel model with the feedback control units captures all important features of the system except the control unit mounting resonances that occur for frequencies above 7 kHz. For the control system on the honeycomb panel it is those mounting resonances that impose the stability limit of the system.

6.1.2. Stability of the five control loops

Figs. 17 and 18 show the eigenvalues of the fully populated matrices with the sensor-actuator open-loop response functions between all sensor outputs and the inputs to the control boards driving each actuator, for the control system mounted on the aluminium and honeycomb panels, respectively. The eigenvalue loci for the control system mounted on the aluminium panel shown in Fig. 17(b) have the same low frequency characteristics as the OL-FRFs for the individual feedback loops in Fig. 15. However, all circles are slightly inflated and the low frequency circle of one eigenvalue crosses the negative real axis close to the Nyquist stability point. This shows that although all individual control loops have a gain margin of 6 dB, the resulting control system with five decentralised control loops is only marginally stable.

Also the eigenvalues for the control system mounted on the honeycomb panel given in Fig. 18(b) show similar characteristics to the OL-FRFs for the individual feedback loops in Fig. 16(b). The low frequency circles on the left half-plane of the Nyquist plot are slightly inflated, which may be due to numerical instability in the eigenvalue computation. As discussed for the OL-FRFs of the individual feedback loops in Fig. 15, it is the high frequency part of the eigenvalues that limit the gain margin and determine the control spillover. The high frequency loci of the eigenvalues in the Nyquist plot in Fig. 18(b) are only very slightly inflated compared with those in Fig. 16(b), which indicates only little cross-talk between the individual feedback loops at these high frequencies. Thus multiple feedback loops can be implemented with control gains close to those that could implemented if the control units were operating in isolation.

6.2. Control performance

This section presents the measured narrow-band spectra of the panel kinetic energy and radiated sound power for the aluminium and the honeycomb panel. The results presented are those for the panels without control units, the panels with open-loop control units and for the active panels with manually tuned feedback control gains. The feedback gain for each

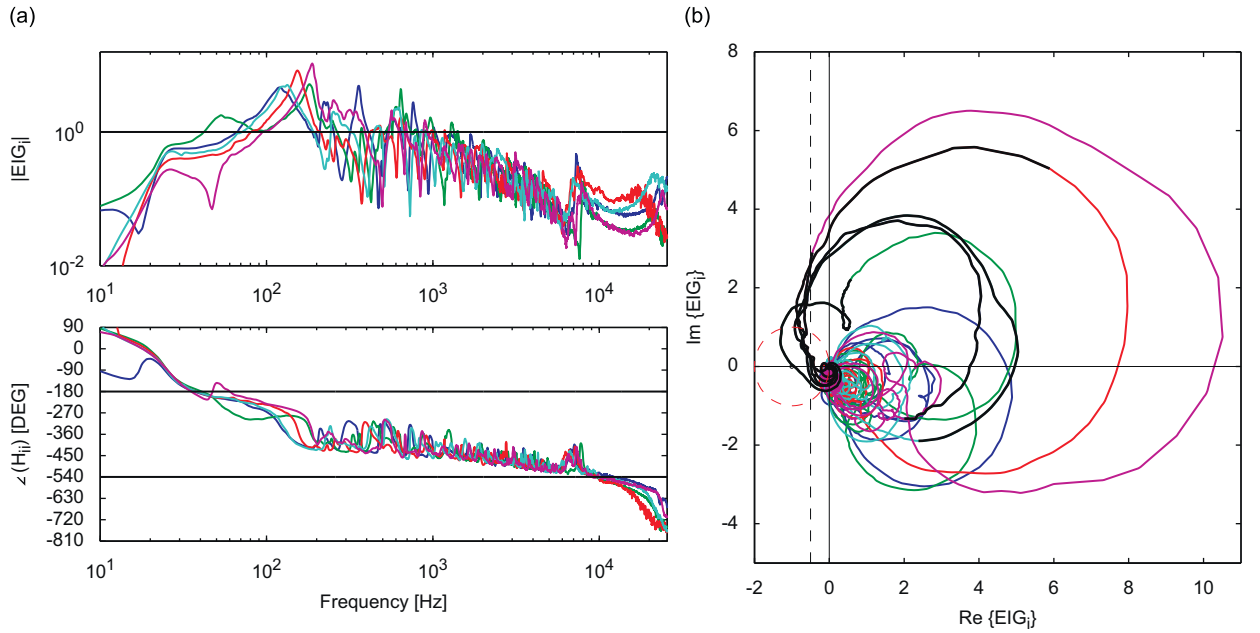

Fig. 17. Eigenvalues of the open-loop FRF matrix of the control system on the aluminium panel. Thick solid lines in the Nyquist plot mark the FRFs in the frequency range from 0 to 150 Hz and the (*dashed*) lines mark the 6 dB gain margin limit and the unit circle around the Nyquist stability point.

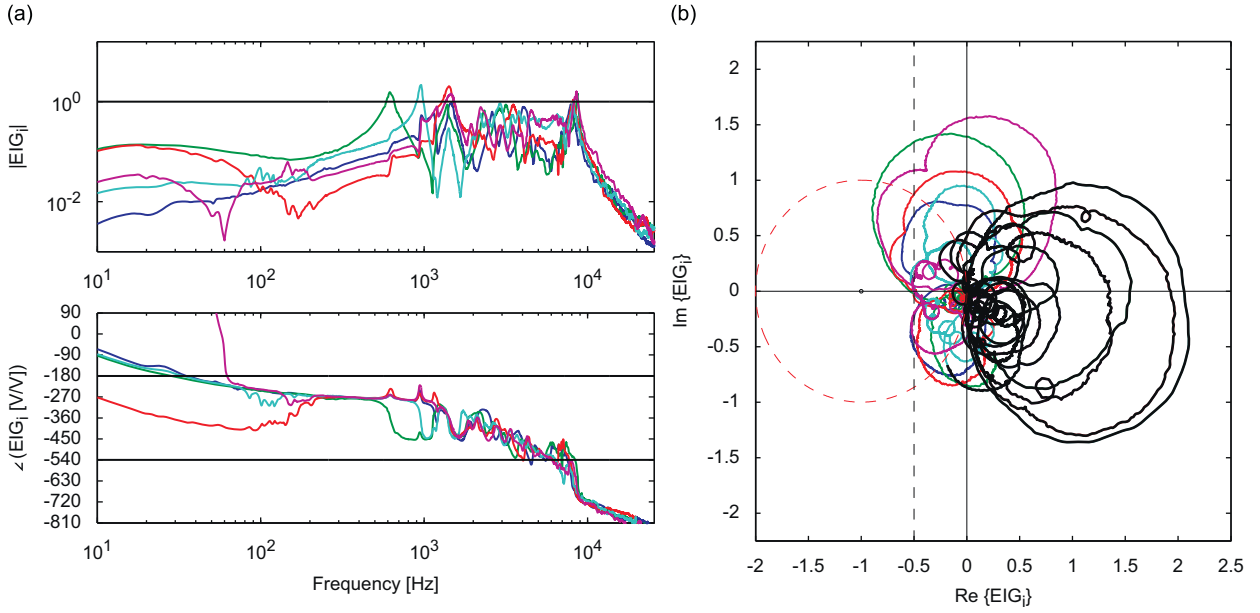

Fig. 18. Eigenvalues of the open-loop FRF matrix of the control system on the honeycomb panel. Thick solid lines in the Nyquist plot mark the FRFs in the frequency range from 0 to 3000 Hz and the (*dashed*) lines mark the 6 dB gain margin limit and the unit circle around the Nyquist stability point.

control unit has been individually tuned to the maximum gain that guaranteed the system to be stable when mounted either on the aluminium (feedback gain limited due to low frequency instability) or the honeycomb panel (feedback gain limited due to high frequency control spillover; gain adjusted such that the control spillover was not audible).

6.2.1. Shaker excitation

The plots in Fig. 19 show the measured narrow-band spectra of the panel kinetic energy and radiated sound power for the aluminium panel (left hand side) and the honeycomb panel (right hand side) with shaker excitation. Fig. 20 shows the

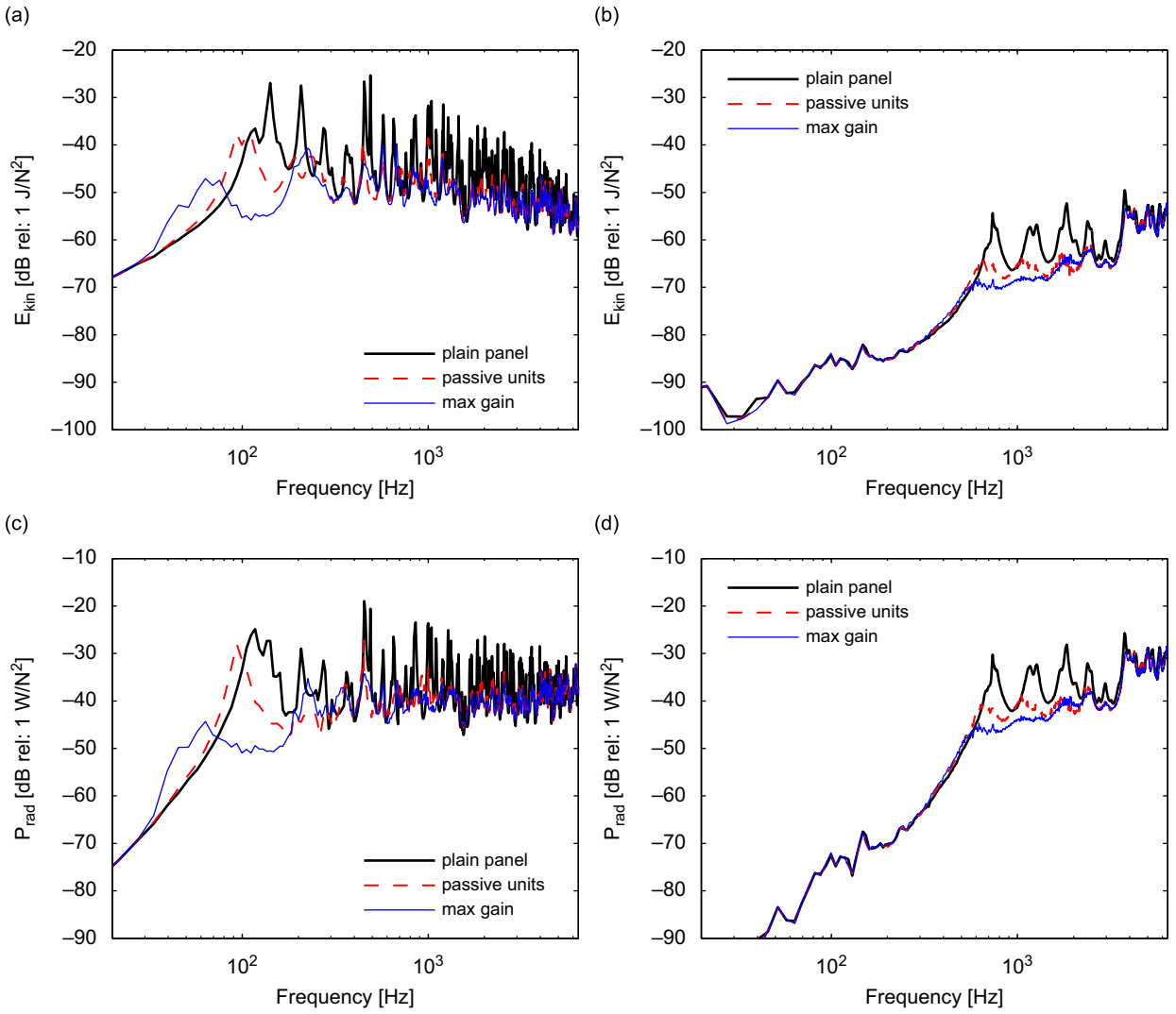

Fig. 19. Measured kinetic energy (*top plots*) and sound power radiated (*bottom plots*) for shaker excitation. Aluminium panel (*left*) and honeycomb panel (*right*); panel kinetic energy (*top*) and radiated sound power (*bottom*).

corresponding changes in panel kinetic energy and radiated sound power in 1/3 octave bands for the panels with passive control units and with closed feedback loops in each case relative to the spectra of the plain panels.

Considering first the narrow-band kinetic energy spectra for the plain panels in Figs. 19(a) and (b), it can be observed that for low and mid frequency bands the spectra for both panels are characterised by a set of well-separated resonances of low order modes; those of the aluminium panel occur between the fundamental frequency of 117 Hz and about 500 Hz, while those of the honeycomb panel occur between the fundamental resonance at 735 Hz and about 2000 Hz.

For higher frequencies, the kinetic energies of the two panels are characterised by more complex spectra resulting from the response of a number of overlapping modes. The kinetic energy spectrum of the honeycomb panel shows a dip between 3000 and 3800 Hz, which is due to the uneven frequency distribution of resonance frequencies of the anisotropic honeycomb panel and the location of the primary force position, which was predicted in the simulation study. For frequencies below 3800 Hz the kinetic energy of the plain aluminium panel is much higher than that of the plain honeycomb panel.

As found in the simulation studies in Section 5, the measured sound radiation spectrum of the aluminium panel is characterised by many resonance peaks and anti-resonance troughs which are due to the low order structural modes that poorly radiate sound below the acoustic critical frequency at about 7500 Hz. In contrast at low and mid audio frequencies the sound radiation of the honeycomb panel is characterised by a few well-separated resonances, due to low order efficiently radiating modes, which resonate above the acoustic critical frequency of about 400 Hz.

The plots in Fig. 19 also show the measured responses and sound radiation spectra of the two panels with attached open-loop and closed-loop velocity feedback control units. The passive effects of the open-loop control units shift the resonance

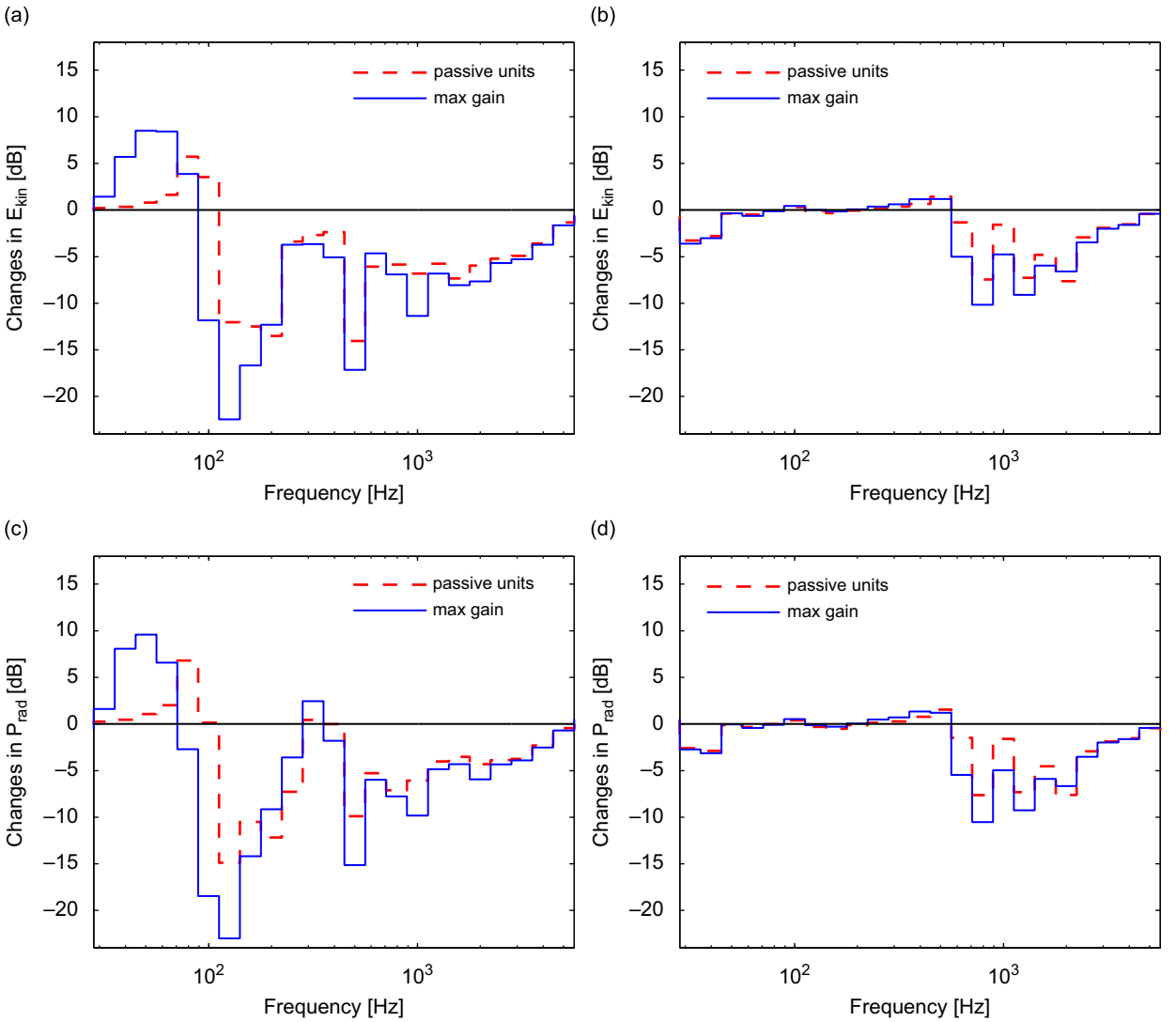

Fig. 20. Change in the panel kinetic energy (*top plots*) and radiated sound power (*bottom plots*) for shaker excitation, evaluated in 1/3 octave bands. Aluminium panel (*left*) and honeycomb panel (*right*); E_{kin} (*top*) and P_{rad} (*bottom*).

frequencies of low order modes downwards, due to the added masses. Also, the amplitudes of the resonant modes are significantly reduced over a wide frequency range due to passive damping effects. Above the fundamental resonance of the actuators, the magnet proof-mass acts as an inertial reference so that, as described in Section 5, both mechanical and electrical damping effects are produced. The shift of low frequency resonances and the broad-band damping effects due to the passive action of the control actuators can also be seen in the 1/3 octave band spectra in Fig. 20.

Compared to the predicted responses in Fig. 10 (structural parameters estimated from measurements on the freely supported honeycomb panel), the measured responses of low order structural modes of the honeycomb panel when mounted in the test frame have a significantly lower magnitude. It is assumed that this is due to the mounting conditions of the honeycomb panel in the test frame, which affects the dynamics of the sandwich structure and also introduces boundary losses (the estimated total loss factors of low order modes vary between about 2 percent and 10 percent). For increasing frequency the magnitude of the response is increasingly similar to that predicted numerically. Also above 3800 Hz the magnitudes of the response of both the honeycomb and aluminium panels approach similar levels.

Moving to the sound radiation spectra shown in Figs. 19(c) and (d), in contrast to what is found for the kinetic energy, above the fundamental resonance frequency of the honeycomb panel at 735 Hz, both panels show similar sound radiation levels. This is due to the fact that the two panels have significantly different radiation efficiencies at low and mid audio frequencies, which, combined with the different response levels at these frequencies, give rise to similar sound radiation levels.

As shown on the left hand side of Figs. 19 and 20, for the aluminium panel with closed-loop feedback control units, additional reductions of both kinetic energy and radiated sound power are achieved in the frequency range from 80 to

200 Hz. In particular, in the 125 Hz 1/3 octave band that contains the panel fundamental resonance frequency, the kinetic energy and radiated sound power reduced by more than 10 dB to give a total reduction due to active and passive effects of more than 20 dB. In the frequency region between 20 and 63 Hz, the feedback control results in enhancement of the panel response and radiated sound power; particularly in the 50 Hz 1/3 octave band the panel kinetic energy and radiated sound power are increased by about 10 dB. This is due to the control spillover effects around the fundamental resonance of the actuators as discussed in Sections 5.1 and 6.1.

As shown on the right hand side plots of Figs. 19 and 20, for the honeycomb panel with closed-loop feedback control units, additional reductions of both kinetic energy and radiated sound power are achieved in the frequency range between 630 and 1600 Hz. In particular in the 800 Hz 1/3 octave band that contains the panel fundamental resonance frequency, the kinetic energy and radiated sound power are reduced by about 4 dB to give a total reduction, due to passive and active effects, of more than 10 dB. It would be possible that passive treatment such as constrained layer damping could be used to give reductions at these higher frequencies. However, due to the large wavelength and the high initial damping these would not be expected to be particularly efficient in the present case. Below 500 Hz the response of the honeycomb panel is stiffness-controlled and drops rapidly as frequency decreases. Therefore, as discussed in Sections 5.1 and 6.1, only little low frequency control spillover is produced by the closed-loop control units.

6.2.2. *Loudspeaker excitation*

Considering loudspeaker excitation the plots in Fig. 21 show the measured narrow-band spectra of the kinetic energy and radiated sound power for the aluminium panel (left hand side) and the honeycomb panel (right hand side). Results are

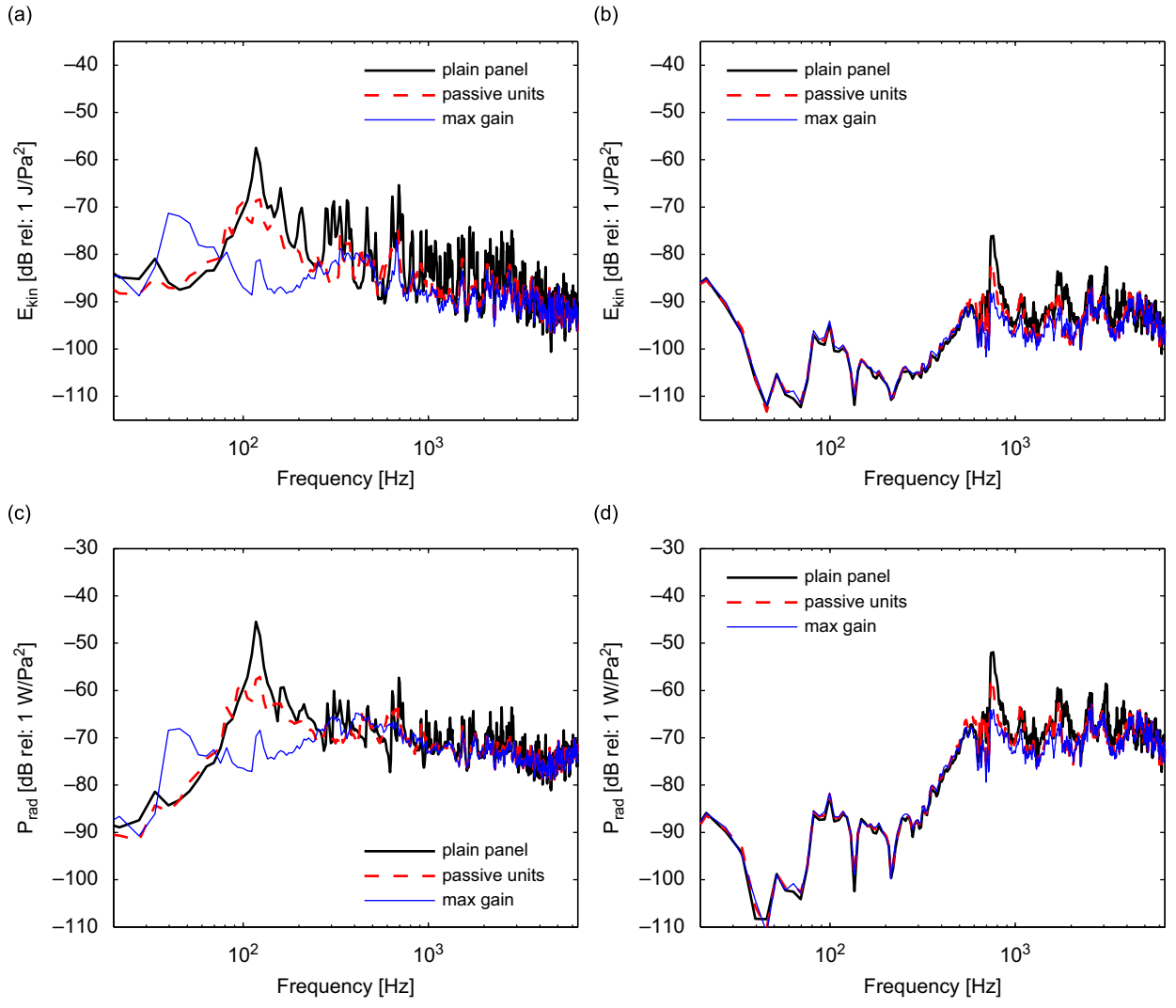

Fig. 21. Measured kinetic energy (*top plots*) and sound power radiated (*bottom plots*) for loudspeaker excitation. Aluminium panel (*left*) and honeycomb panel (*right*); panel kinetic energy (*top*) and radiated sound power (*bottom*).

presented for the panels without control units, the panels with open-loop control units and for the active panels with manually tuned feedback control gains. Fig. 22 shows the changes in panel kinetic energy and radiated sound power in 1/3 octave bands.

The narrow-band kinetic energy spectra for loudspeaker excitation, in Figs. 21(a) and (b), show similar characteristics to those found for the shaker excitation, although they are characterised by a smaller number of well-separated resonances and also tend to roll off at a higher rate as frequency increases. This is due to the fact that the distributed acoustic field does not efficiently excite all low order modes and also the excitation strength tends to decrease with increasing frequency, a characteristic also seen in the simulation results, shown in Fig. 12. Compared with the results for shaker excitation, below 3800 Hz the kinetic energy of the plain honeycomb panel excited by the loudspeaker is closer to that for the aluminium panel. This is because the structural modes of the honeycomb panel are more efficiently excited by the acoustic field produced by the loudspeaker.

The narrow-band radiated sound power spectra for loudspeaker excitation in Figs. 21(c) and (d) show that above 735 Hz the radiated sound power of the plain honeycomb panel exceeds that of the aluminium panel. This confirms the predicted combined effect of higher radiation efficiency and higher sensitivity to acoustic disturbance of the honeycomb panel resonant modes.

As shown in Figs. 21 and 22, for loudspeaker excitation, the sound radiation from the aluminium panel above 400 Hz is only marginally changed by the passive and active effects of the control units. This is because the radiated sound power spectrum is mass-controlled and not dominated by resonant modes.

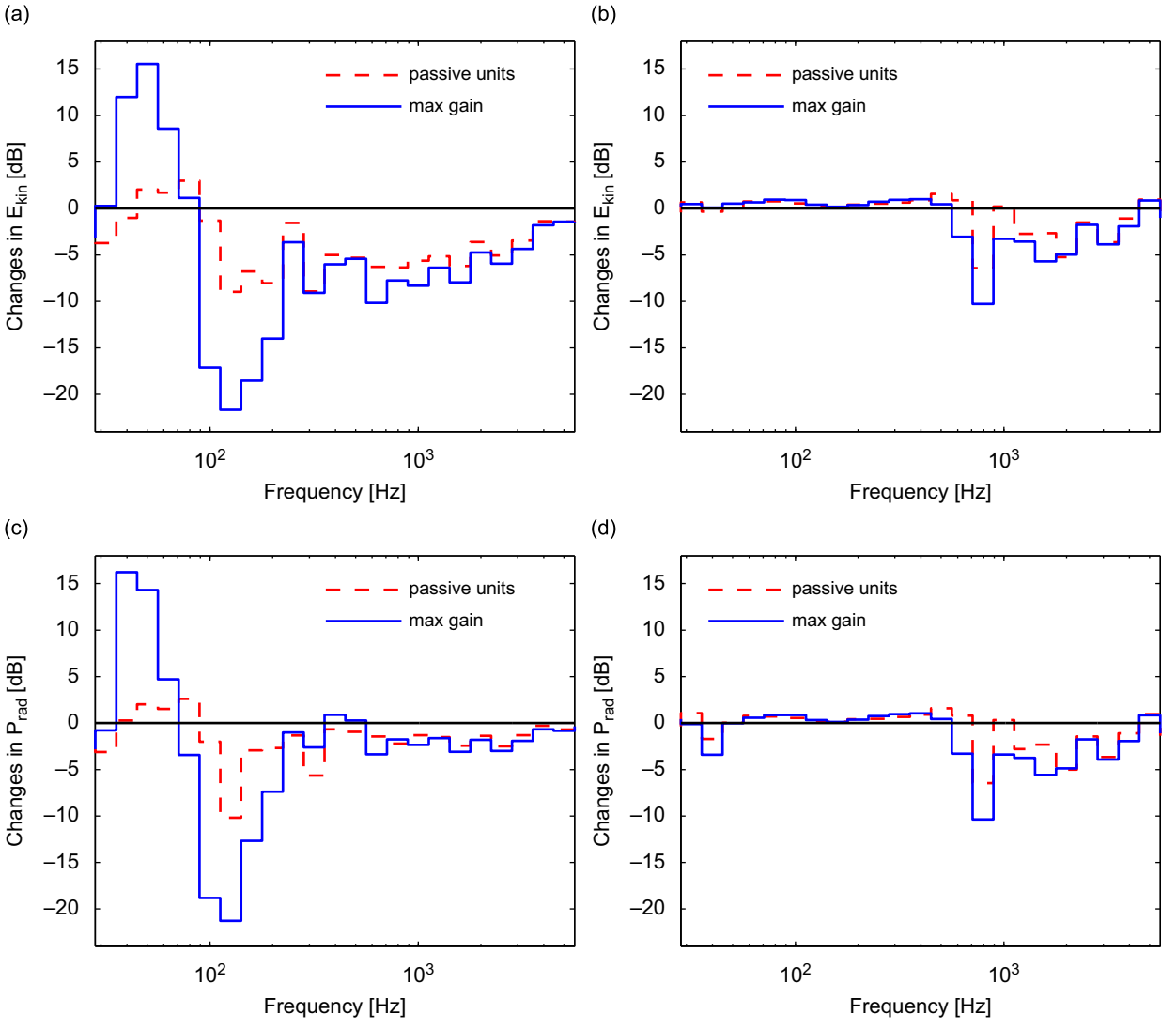

Fig. 22. Change in the panel kinetic energy (*top plots*) and radiated sound power (*bottom plots*) for loudspeaker excitation, evaluated in 1/3 octave bands. Aluminium panel (*left*) and honeycomb panel (*right*); E_{kin} (*top*) and P_{rad} (*bottom*).

Comparison of the changes in kinetic energy and radiated sound power in Figs. 20 and 22 shows that the reductions achieved for both types of excitation are otherwise very similar. The experimental studies confirm that the reductions achieved depend on the number of modes that are efficiently excited at resonance and, for the sound power, also on the number of modes that radiate sound efficiently.

7. Conclusions

Simulation and experimental measurements have been carried out in order to assess and compare the control stability and performance of a decentralised velocity feedback control system with five proof-mass electrodynamic actuator—accelerometer pairs when installed on a thin homogeneous aluminium panel and a stiff honeycomb sandwich panel. The control stability has been analysed in terms of the sensor-actuator open-loop frequency response function of the control units with respect to the general Nyquist stability criterion. For both the simulation and experimental studies the control performance has been assessed in terms of panel kinetic energy and radiated sound power of the two panels. The experimental measurements validate the simulation results. The active panel model used in the simulation study captures all important physical effects. The two panels are characterised by a very similar mass per unit area, but the honeycomb panel has a much higher bending stiffness than the aluminium panel. Thus the bending wavenumbers on the honeycomb panel are significantly lower than those of the aluminium panel in the entire frequency range of interest. This results in considerably different fundamental resonance and acoustic coincidence frequencies. It also results in a much lower modal density and in a much lower acoustic critical frequency for the honeycomb panel. Due to its lower fundamental resonance frequency, the response and radiated sound power of the plain aluminium panel at low audio frequencies are much higher than those of the plain honeycomb panel. Moreover, although the passive and active effects of the five control units efficiently reduce the response and the radiated sound power of the aluminium panel at low frequencies, those reductions are not significant enough to bring down the response and sound radiation levels to those observed for the honeycomb panel. In the mid audio frequency range, all modes of the honeycomb panel are efficient radiators of sound and are also efficiently excited by an acoustic source, which results in higher levels of radiated sound power than for the aluminium panel. However, it has been found that the control loops perform better on the honeycomb panel in terms of both control stability and control performance. As a result, depending on the type of excitation, the response and radiated sound power of the honeycomb panel in the mid audio frequency range can be controlled to similar or even lower levels than those of the aluminium panel. The results in this paper indicate a high potential for the application of velocity feedback control to reduce the kinetic energy and radiated sound power of stiff sandwich panels. Active control technology could balance the poor sound transmission properties of lightweight sandwich structures to such an extent that this may justify the additional expense and additional installed mass of active control systems.

Acknowledgements

This research work was supported by an EU 'Marie Curie Fellowship for Early Stage Research Training' within the 'European Doctorate Sound and Vibration Studies' (EDSVS) programme. The authors would also like to thank Armando Vavalle from GKN Aerospace Ltd for his assistance and for providing the honeycomb test panel used in the experimental study.

References

[1] J.S. Mixson, J.F. Wilby, Interior Noise, *Aeroacoustics of Flight Vehicles, Theory and Practice*, Chapter 16, NASA Langley Research Center, Hampton, Virginia, 1995.
[2] J.F. Wilby, Aircraft interior noise, *Journal of Sound and Vibration* 190 (3) (1996) 545–564.
[3] P. Gardonio, Review of active techniques for aerospace vibro-acoustic control, *Journal of Aircraft* 39 (2) (2002) 206–214.
[4] D.J. Thompsonn, J. Dixon, Vehicle noise, in: F.J. Fahy, J.G. Walker (Eds.), *Advanced Applications in Acoustics, Noise and Vibration*, E & FN Spon, London and New York, 2004 (Chapter 6).
[5] D.J. Thompson, *Railway Noise and Vibration. Mechanisms, Modelling and Means of Control*, Elsevier Science, Oxford, UK, 2008.
[6] F.J. Fahy, Fundamentals of noise and vibration control, in: F.J. Fahy, J.G. Walker (Eds.), *Fundamentals of Noise and Vibration*, E & FN Spon, London, 1998 (Chapter 5).
[7] M.J. Brennan, N.S. Ferguson, Vibration control, in: F.J. Fahy, J.G. Walker (Eds.), *Advanced Applications in Acoustics, Noise and Vibration*, E & FN Spon, London and New York, 2004 (Chapter 12).
[8] D.J. Mead, *Passive Vibration Control*, John Wiley, Chichester, UK, 1998.
[9] J. Rohlfing, P. Gardonio, Homogeneous and sandwich active panels under deterministic and stochastic excitation, *Journal of the Acoustical Society of America* 125 (6) (2009) 3696–3706.
[10] M. Balas, Direct velocity feedback control of large space structures, *Journal of Guidance, Control, and Dynamics* 2 (3) (1979) 252–253.
[11] F.J. Fahy, P. Gardonio, *Sound and Structural Vibration Radiation Transmission and Response*, second ed., Academic Press, Oxford, 2007.
[12] A. Preumont, *Mechatronics Dynamics of Electromechanical and Piezoelectric Systems*, Springer, Dordrecht, The Netherlands, 2006.
[13] C. Paulitsch, P. Gardonio, S. Elliott, Active vibration control using an inertial actuator with internal damping, *Journal of the Acoustical Society of America* 119 (4) (2006) 2131–2140.
[14] C. Paulitsch, P. Gardonio, S.J. Elliott, Active vibration damping using an inertial electrodynamic actuator (detc2005-84632), *Journal of Vibration and Acoustics, Transactions of the ASME* 129 (1) (2007) 39–47.
[15] S.J. Elliott, M. Serrand, P. Gardonio, Feedback stability limits for active isolation systems with reactive and inertial actuators, *Journal of Vibration and Acoustics, Transactions of the ASME* 123 (1) (2001) 250–261.

[16] C. Gonzalez-Diaz, C. Paulitsch, P. Gardonio, Active damping control unit using a small scale proof mass electrodynamic actuator, *Journal of the Acoustical Society of America* 124 (2) (2008) 886–897.
[17] A. Preumont, *Vibration Control of Active Structures*, Kluwer Academic Publisher, Dordrecht/Boston/London, 2002.
[18] S. Elliott, *Signal Processing for Active Control*, Academic Press, London, 2001.
[19] J. Rohlfing, P. Gardonio, Active control of sound transmission through panels with flexible boundaries under deterministic and stochastic excitation, University of Southampton, Institute of Sound and Vibration Research, Technical Memorandum No. 977, 2007.
[20] P. Gardonio, S.J. Elliott, Smart panels for active structural acoustic control, *Smart Materials and Structures* 13 (6) (2004) 1314–1336.
[21] G.B. Warburton, The vibration of rectangular plates, *Proceedings of the Institution of Mechanical Engineers* 168 (1954) 371–384.
[22] P. Gardonio, M.J. Brennan, Mobility and impedance methods in structural dynamics, in: F.J. Fahy, J.G. Walker (Eds.), *Advanced Applications in Acoustics, Noise and Vibration*, E & FN Spon, London and New York, 2004 (Chapter 9).
[23] E. Nilsson, A.C. Nilsson, Prediction and measurement of some dynamic properties of sandwich structures with honeycomb and foam cores, *Journal of Sound and Vibration* 251 (3) (2002) 409–430.
[24] C.W. Schwingshackl, G.S. Aglietti, P.R. Cunningham, Determination of honeycomb material properties: existing theories and an alternative dynamic approach, *Journal of Aerospace Engineering* 19 (3) (2006) 177–183.
[25] R.D. Blevins, *Formulas for Natural Frequency and Mode Shape*, Robert E. Krieger, Malabar, Florida, 1984.
[26] J.J. Tuma, R.A. Walsh, *Engineering Mathematics Handbook*, fourth ed., McGraw-Hill, New York, NY, 1997.
[27] J. Rohlfing, Decentralised Velocity Feedback Control for Thin Homogeneous and Lightweight Sandwich Panels, PhD Thesis, University of Southampton, 2009.
[28] C. González Díaz, P. Gardonio, Feedback control laws for proof-mass electrodynamic actuators, *Smart Materials and Structures* 16 (5) (2007) 1766–1783.
[29] C. González Díaz, C. Paulitsch, P. Gardonio, Smart panel with active damping units. Implementation of decentralized control, *Journal of the Acoustical Society of America* 124 (2) (2008) 898–910.
[30] O.N. Baumann, S.J. Elliott, The stability of decentralized multichannel velocity feedback controllers using inertial actuators, *Journal of the Acoustical Society of America* 121 (1) (2007) 188–196.
[31] C. Hong, Active Control of Resiliently-Mounted Flexible Structures, PhD Thesis, University of Southampton, 2005.